Multi-stage metamorphic and metasomatic imprints on apatite-monazite-xenotime assemblages in a set of small iron oxide-apatite (IOA) ore bodies, Prins Karls Forland, Svalbard

Maria Maraszewska [a,b], Jarosław Majka [c,d,*], Daniel E. Harlov [e,f,g], Maciej Manecki [c,d], David A. Schneider [h], Igor Broska [a], Per-Inge Myhre [i]

[a] *Earth Science Institute, Slovak Academy of Sciences, Bratislava, Slovakia*
[b] *Faculty of Natural Sciences, Commenius University, Bratislava, Slovakia*
[c] *Department of Earth Sciences, Uppsala University, Uppsala, Sweden*
[d] *Faculty of Geology, Geophysics and Environmental Protection, AGH University of Science and Technology, Kraków, Poland*
[e] *Deutsches GeoForschungs Zentrum GFZ, Telegrafenberg, 14473 Potsdam, Germany*
[f] *Faculty of Earth Resources, China University of Geosciences, Wuhan 430074, China*
[g] *Department of Geology, University of Johannesburg, P.O. Box 524, Auckland Park 2006 South Africa*
[h] *Department of Earth and Environmental Sciences, University of Ottawa, Ottawa, Canada*
[i] *Norwegian Polar Institute, Tromsø, Norway*

ARTICLE INFO

ABSTRACT

On Prins Karls Forland, Svalbard Archipelago, a set of small iron oxide-apatite (IOA) ore bodies have been discovered within a crustal shear zone, which deformed the polymetamorphosed Neoproterozoic metasedimentary rocks. The ores have various styles and grades of deformation and distinct mineral assemblages whose compositions record a multi-stage tectonothermal and metasomatic history. These IOA ore bodies can be subdivided into fluorapatite-bearing and predominant low-Th monazite in the upper section of the shear zone and F-Cl apatite-bearing and predominant high Th-monazite in the structurally lower higher-grade deformed part. The first stage of alteration for these ore bodies resulted in metasomatic alteration of the apatite and liberation of REE and P redeposited as monazite and xenotime. The transport of dissolved REE and P was likely enhanced by deformation. The second stage of alteration had a distinct impact on the individual ore bodies, which resulted in the Th-enrichment of a small subset of the monazite grains in the upper section of the shear zone. In the lower section of the shear zone most of the monazite was replaced by high Th monazite. Here the original fluorapatite is enriched in Cl, Mn, and Sr, most probably due to interaction with $CaCl_2$-rich fluids enriched in Sr and Mn that was scavenged from the hosting metasediments and altered metagabbros. Contrasting textures, mineral assemblages, and the geochemistry of the ores from distinct localities reflect involvement of compositionally different fluids from the gabbroic rocks and surrounding metasedimentary rocks during the protracted tectonothermal evolution of Prins Karls Forland. Therefore, it is concluded that the IOA ore bodies most likely resulted due to the fractionation of Fe, P, Ca, and REE from hypersaline fluids associated with the gabbros. Once deposited, these IOA ore bodies were subsequently altered during at least one and perhaps two later metamorphic events.

1. Introduction

Kiruna-type or iron oxide-apatite (IOA) ore bodies occur through geological time and are globally found generally associated with subvolcanic formations. The classic locality for such deposits is the Paleoproterozoic Kirunavaara district in northern Sweden (Geijer, 1910, 1931, 1967; Cliff et al., 1990; Romer et al., 1994; Harlov et al., 2002), where the extensive ore body is hosted by calc-alkaline rhyodacytes and trachytes (Perdahl and Frietsch, 1993). However, similar deposits of the same age are also known from other localities within the Fennoscandian Shield, such as the Grängesberg district in central Sweden (Jonsson et al., 2011, 2013, 2016). Other notable IOA localities include the Pea

---

Ridge deposit in southeast Missouri, USA (e.g. Harlov et al., 2016), the Bafq region in Iran (Daliran, 2002; Taghipour et al., 2015), the Middle-Lower Yangtze River metallogenetic belt in China (Hu et al., 2019), and a series of deposits within the Chilean Iron Belt, such as El Laco and Los Colorados (Nyström and Henríquez, 1994; Tornos et al., 2017). In all these cases the ores are associated with subvolcanic or volcanic calc-alkaline formations, and to a lesser extent with plutonic systems, predominantly felsic or intermediate in character, in a volcanic arc or back-arc or continental rift setting (Oyarzun et al., 2003; Allen et al., 1996).

The two principal models for IOA ore deposition and mineralisation invoke either a fluid-aided or an orthomagmatic origin. The fluid model states that late-magmatic, metamorphic, or/and surficial fluids were responsible for the transport and emplacement of magnetite and apatite, which metasomatically replaced the original minerals in these deposits (Ménard, 1995; Sillitoe and Burrows, 2002; Dare et al., 2015). Magmatic genesis is proposed to be due to the immiscibility between siliceous and volatile-saturated Fe-P ore cumulates from a silicic magma (Nyström and Henríquez, 1994; Jonsson et al., 2013; Hou et al., 2018). A compromise between these two models combines a magmatic origin with post-magmatic alteration where the ores represent late-stage fractionated igneous derived bodies affected by concurrent multistage metasomatism (Knipping et al., 2015; Jonsson et al., 2016; Harlov et al., 2016; Hu et al., 2019). The recent correlation of Fe and O isotopes from IOA localities worldwide support an orthomagmatic origin for the magnetite, coupled with the influence of a metasomatic overprint (Troll et al., 2019; Knipping et al., 2019).

The fluids involved in the formation of IOA ores are dominantly magmatic in origin and related to late-stage exsolution from a fluid-saturated residual melt facilitated by a decrease in the temperature and pressure during emplacement. The concentration of volatiles during the progressive differentiation of igneous magmas is the principal factor controlling the distribution of magmatic-hydrothermal ore deposits in general (e.g. Williams-Jones and Heinrich, 2005). The estimated temperatures for magnetite crystallization in these IOA ore bodies ranges from >800 °C to <200 °C, and reflects the transition from a high-temperature, purely magmatic to a purely fluid-thermal environment; moreover, the later stages after emplacement can also involve metasomatic alteration due to external fluids (Troll et al., 2019; Palma et al., 2020).

The composition of the fluids associated with IOA ore deposits varies between particular localities but also between stages of ore system evolution. In general, orthomagmatic fluids are predominantly halogen-rich, i.e. high salinity, and oxidised (Smith et al., 2013; Palma et al., 2020; Shu et al., 2021). The origin and chemistry of the fluids involved in their metasomatic alteration is generally unique per IOA deposit. This reflects variations in the composition of the source rocks (from felsic to mafic, alkaline to subalkaline, etc.) and the hosting lithologies coupled with their respective volatile budgets. Last, but not least, a significant factor in the evolution of fluids and the pathways of their flow within the crust is the tectonic and metamorphic history of the area, since deformation and metamorphism are linked with the generation and circulation of volatiles within the crust (e.g. Putnis and Austrheim, 2010; Yardley and Cleverley, 2013).

The most characteristic feature of IOA-type mineralisation is an assemblage of iron oxides (Ti-poor magnetite with late hematite) and lesser apatite, which have experienced pervasive metasomatism. Apatite occurs almost exclusively as fluorapatite with minor amounts of Cl and OH (Harlov et al., 2002; Torab and Lehmann, 2007; Jonsson et al., 2016; Harlov et al., 2016). However, Cl-rich varieties of apatite have also been described in some deposits from northern Chile (Treloar and Colley, 1996; La Cruz et al., 2019; Palma et al., 2019), and in zoned apatite from the Se-Chahun deposit in the Bafq district (Bonyadi et al., 2011). This enrichment of apatite in Cl or Cl-OH is regarded as a secondary process due to Cl-rich fluids under various pH conditions (Palma et al., 2019) or by mixing between compositionally contrasting fluids from magmatic and supergene sources (Treloar and Colley, 1996).

A second feature of the Kiruna-type apatite is their variable REE content, which ranges from non-existent up to thousands of ppm (Belousova et al., 2002; Mao et al., 2016). Moreover, apatites from different locations are associated with REE-bearing phases such as monazite and xenotime, and locally also allanite, REE-fluorides, and REE-carbonates, which are presumed to have formed by metasomatic alteration of the apatite (e.g. Harlov et al., 2002; Harlov and Förster, 2003; Harlov et al., 2005; Jonsson et al., 2016; Harlov et al., 2016). The scale and abundance of these REE mineral assemblages vary between deposits worldwide. For example, in IOA deposits from the Chilean Iron Belt, REE minerals are nearly non-existent (Palma et al., 2019), whereas in Bafq district or Pea Ridge, the occurrence of REE minerals is both extensive and abundant (Daliran, 2002; Harlov et al., 2016).

This study focuses on the description and interpretation of the mineralogy, petrographic textures, and the geochemistry of oxide-phosphate mineral assemblages in several newly discovered small IOA ore bodies on Prins Karls Forland, an island belonging to the Svalbard Archipelago in the High Arctic. We speculate on an origin of these ore bodies, their relationship to the surrounding rock, and the age of their emplacement and evolution. We then discuss their similarity and unique character in comparison to other IOA deposits worldwide. In a broader context, the specific character of the apatite-monazite-xenotime assemblages in the IOA ores from Prins Karls Forland contribute to a better understanding of the response of REE-bearing minerals to multiple deformation, metamorphic and metasomatic events in general, and the complexity of fluid-mineral interaction from the micron-scale to the regional-scale during a protracted tectono-thermal history.

2. Geological setting

The Svalbard Archipelago is situated in the High Arctic on the northwest edge of the Barents Shelf. Its Caledonian crystalline basement consists of domains (provinces) characterised by distinct tectonostratigraphy and tectonometamorphic history (e.g. Gee and Teben'kov, 2004; Dallmann et al., 2015). Prins Karls Forland (PKF) is a N-S elongated island separated from Spitsbergen by the Tertiary Forlandsundet Graben. It belongs to the Southwestern Basement Province of Svalbard, which is composed of Precambrian to early Paleozoic metamorphosed igneous and sedimentary units. The basement rocks of the Southwestern Province recorded several magmatic and metamorphic episodes from the Mesoproterozoic to the Paleogene (for more details see Majka and Kośmińska, 2017). The whole province was affected by ductile–brittle deformation related to the Tertiary West Spitsbergen Fault and Thrust Belt (Barnes and Schneider, 2019; Schneider et al., 2019). The crystalline basement exposed in the PKF is dominated by low-grade meta-sedimentary sequences, whose correlation with the basement lithologies defined on Spitsbergen is still not well constrained. The IOA ore bodies are situated in the northeast part of the island, in the vicinity of Grimaldibukta (Fig. 1).

The IOA ore bodies occur within a ~1 km wide crustal-scale fault zone called the Boureéfjellet Shear Zone (BSZ; Fig. 1; Schneider et al., 2019), which separates the amphibolite facies Pinkie unit in the west from the overthrusted greenschist facies metaflysch of the Grampianfjella Group (Dallmann et al., 2015; Harland, 1997; Hjelle et al., 1999; Kośmińska et al., 2015; Schneider et al., 2019). In the east, the Pinkie unit is bordered by a normal fault in the low-grade black calcareous slates and phyllonites of the Scotiafjellet Group (Hjelle et al., 1999). Deformation within the BSZ grades from mylonitisation in the lower parts of the profile to cataclasis in the uppermost parts (Schneider et al., 2019). The ductile to brittle deformed lithologies within the BSZ involve the cataclased and mylonitised metasediments of the Pinkie unit and carbonaceous cataclasites of the newly defined Craigtoppane Formation, tentatively ascribed to the Grampianfjella Group (Dallmann, 2020). Local lenses of metagabbroic rocks accompany these main metasedimentary lithologies (Fig. 2a,b). The Craigtoppane Formation, consisting of banded marbles locally with chert, is commonly brecciated in the
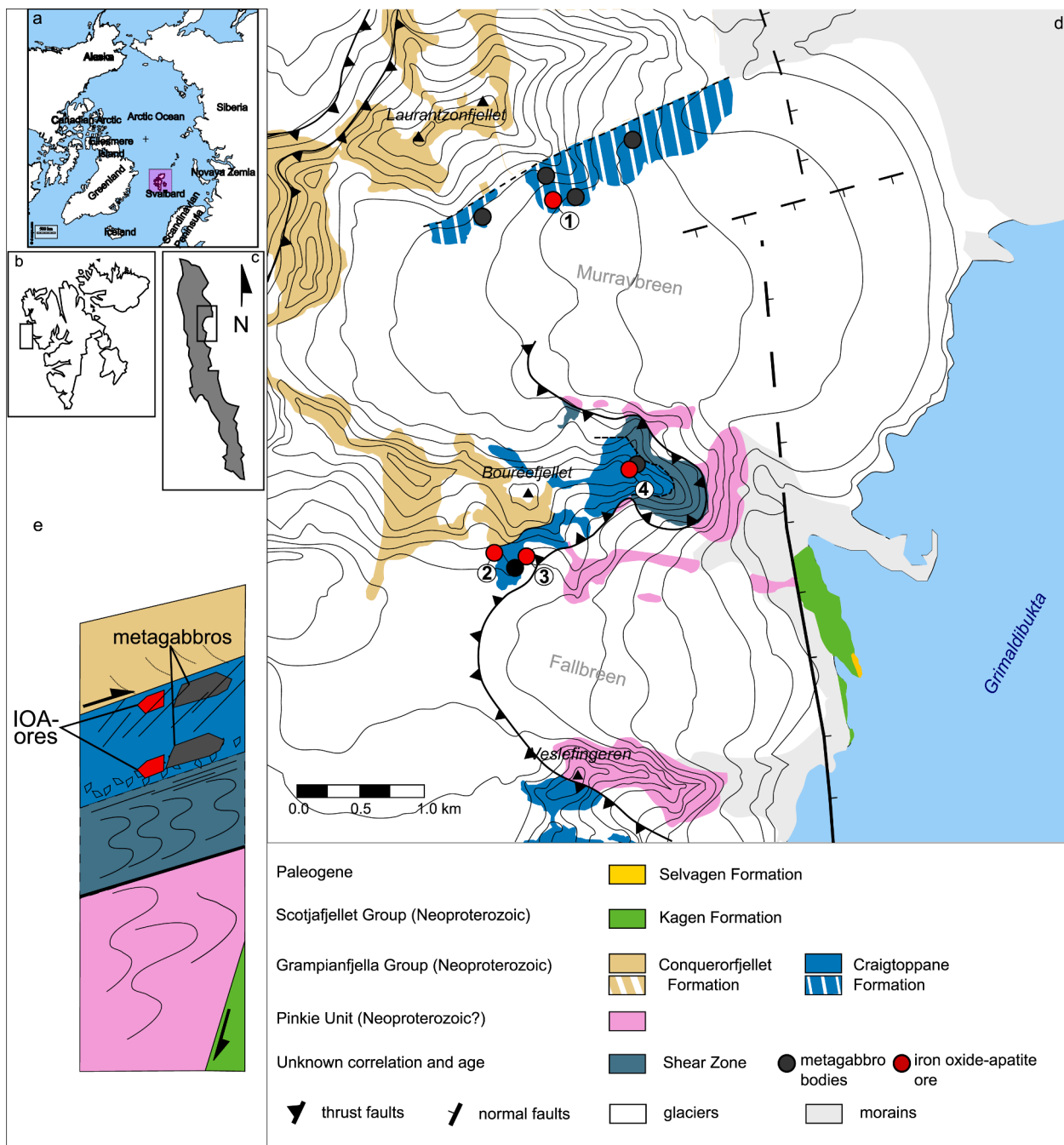
Fig. 1. a) Location of Svalbard Archipelago. b) Location of Prins Karls Forland in the Svalbard Archipelago. c) Investigated area on Prins Karls Forland. d) Simplified geological map of the research area (adapted from Hjelle et al. 1999; Schneider et al. 2019; Dallmann 2020). The ore body numbers refer to the textural types distinguished in Table 1. Diagonal stripes indicate inferred tectonostratigraphic affiliation. e) Schematic profile across the BSZ and Pinkie Unit (modified after Schneider et al. 2019).

form of calcareous cataclasites.

The Pinkie unit is composed of laminated quartzites with carbonaceous bands in its lower part and garnet-bearing mica schists in its upper part (Harland, 1997; Hjelle et al., 1999). The Pinkie metapelite records two stages of garnet formation under amphibolite-facies conditions. The first metamorphic event resulted in garnet, staurolite, and kyanite growth initially from ~560 to 630 °C and 8 to 10 kbar, followed by mylonitisation and the growth of second-generation garnet during the second metamorphic event at ~500 °C and 9 to 11 kbar (Kośmińska et al., 2015). Such relatively high-grade metamorphic conditions are exceptional in the PKF. The scapolite-bearing carbonaceous rocks currently ascribed to the Craigtoppane Formation are estimated to have

formed at 380 to 560° C and 4 to 7.5 kbar (Manby, 1983a, 1986).

Preliminary U-Pb dating of detrital zircons from a quartzite within the Pinkie unit yielded an early Neoproterozoic maximum depositional age of ca. 950 Ma (Kośmińska et al., 2015), whereas monazite Th-U-total Pb dating yielded Ellesmerian ages with a dominant population between 359 ± 6 to 355 ± 14 Ma (Kośmińska et al., 2020). While the first stage of the amphibolite facies metamorphism recorded by the Pinkie unit is unequivocally ascribed to the Ellesmerian tectonism, the exact age of the second stage could be either also Ellesmerian or younger. $^{40}Ar/^{39}Ar$ dating of foliation defining white mica suggests deformation related to Eurekan tectonism (55–45 Ma; Schneider et al., 2019). In the mylonitised lower part of the shear zone, the resetting of the white mica was
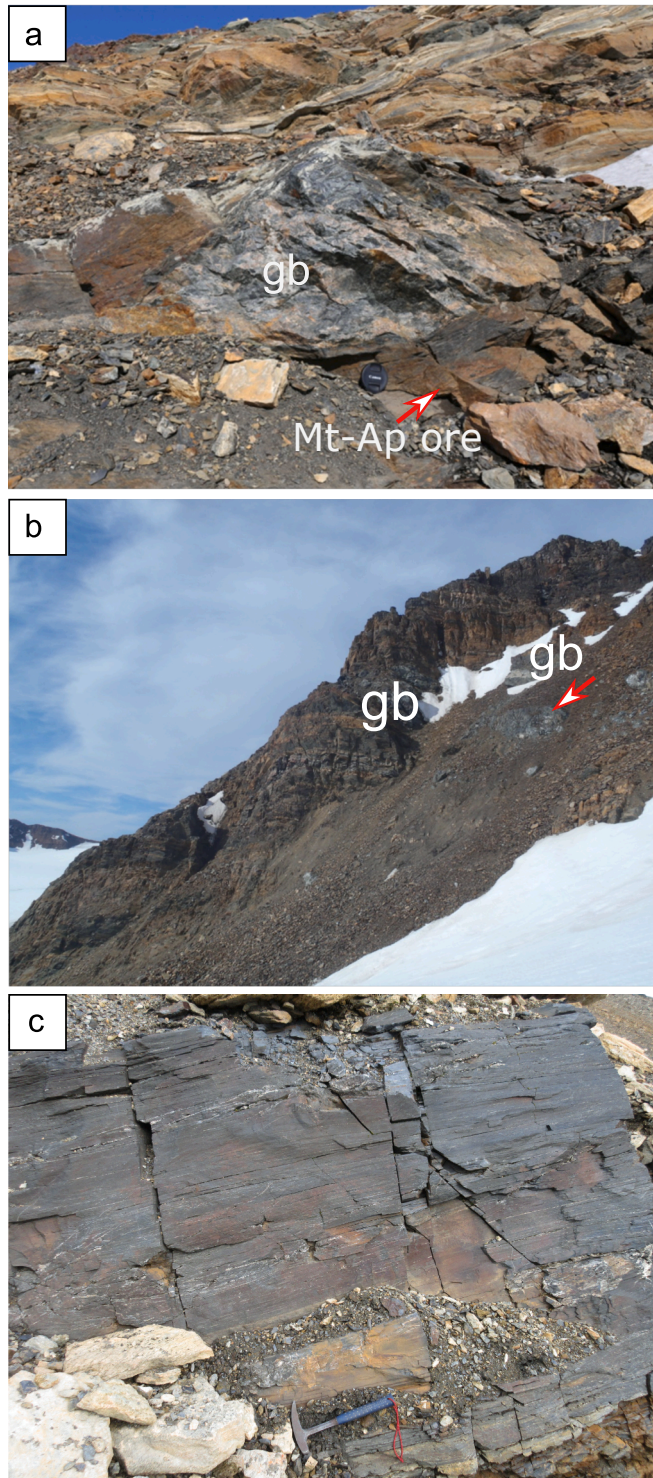
Fig. 2. Field photographs of the PKF IOA ore bodies. a) Lensoidal meta-gabbro body (gb) within metasediments of the Craigtoppane Unit in sharp tectonic contact with a Type (1) ore body (south slope of Laurantzonfjellet). b) Lensoidal-shape boudin of Type (3) ore in spatial association with meta-ferrogabbros (gb) within cataclased calcareous and silicious metasediments (south pillar of Boureéfjellet). The red arrow points to IOA ore bodies. c) Outcrop of banded Type (2) ore emplaced in slaty silicious metasediments. Note the pronounced slaty cleavage of the ore body. Mineral abbreviations: Mt – magnetite, Ap – apatite.

total, whereas in the upper parts dispersed $^{40}Ar/^{39}Ar$ ages indicate partial recrystallisation of the mica. The rocks had cooled to <200 °C by ca. 20 Ma as recorded by zircon (U-Th/He) dates (Barnes and Schneider, 2019).

The second stage of metamorphism was coeval with fluid circulation within the BSZ, which resulted in the development of apatite + allanite coronas around some monazite grains in the garnet-bearing mica schists (Kośmińska et al., 2020), and an abundance of scapolite in the cataclased quartzites and metacarbonates (Manby, 1983b). The non-coaxial strain fabric exhibited by the altered monazites in the schist suggests that the formation of apatite + allanite was pre- to *syn*-tectonic with the shearing and involved Ca- and F-rich fluids. These phenomena occurred broadly coeval with the second metamorphic event described by Kośmińska et al. (2020).

2.1. IOA ore bodies

Lensoidal or block-like IOA ore bodies varying in size from < 1.0 × 1.0 m to 20 × 10 m are found in three localities (Fig. 1; Table 1): (1) on the southern slope of Laurantzonfjellet Fig. 2a (MAG-1; point no. 1 on Fig. 1), (2) as vertical pillars in the southern part of the Boureéfjellet summit (MAG-2; Fig. 2b and MM-18:1B; Fig. 2c; points 3 and 2 on Fig. 1, respectively), and (3) on the western edge of the Boureéfjellet ridge (MAG-3; point 4 on Fig. 1). The ore occurrences at Boureéfjellet were originally discovered by the Scottish Spitsbergen Syndicate Expedition (Tyrrell, 1924), whereas the other ores described herein represent new discoveries. All of the IOA ore bodies occur within the vicinity of metagabbroic boudins dispersed within the BSZ. The degree of metamorphic and metasomatic overprint of the gabbros varies between localities (Maraszewska et al., 2016). At Laurantzonfjellet, where bodies of meta-igneous rocks occur within low-grade cataclasites, the primary adcumulate structure and magmatic mineral assemblage, consisting of Ti pargasite + plagioclase An_{76-67} + ilmenite + Cl-F apatite, is well preserved. In contrast, metagabbros, which are hosted in the deformed lower parts of the BSZ on Boureéfjellet, experienced extensive cataclasis, local protomylonitisation, as well as pervasive Ca-Na-Cl alteration. Here, the primary magmatic mineral assemblage was replaced by ferro- and magnesiohastingsite-edenite + actinolite + epidote-clinozoisite + albite + biotite + titanite + hematite + scapolite + F-Cl apatite ± allanite. The metagabbros were depleted in Fe, Ti, Al, and K and enriched in Si, Ca, P, Ba, Zr, and REE. The trace element geochemical signature of the metagabbros indicate affiliation with oceanic within-plate-magmatism, suggesting an OIB-type or E-MORB-type parental magma (Maraszewska et al., 2016). Representative whole rock chemistry of the metagabbro and EPMA data of minerals are given in Appendix 1.

3. Analytical methods

3.1. Sample selection

Two hand-size samples representative of each of the ore textural types were taken during field work in 2015 and 2018. These include sample Mag-1 (Type 1 ore); MM-18-1a and b (Type 2 ore); MAG-2 (Type 3 ore); and MAG-3 (Type 4 ore). The mineralogy of each of these samples is summarized in Table 1 and presented in Fig. 1. In addition, five samples of the metagabbros (0.5–1 kg each) were collected. The localities, whole-rock chemistry, and representative mineral composition of these samples are given in Appendix 1. Polished thin sections of these samples were petrographically examined using both transmitted and reflected light on an OLYMPUS-51 optical microscope in the Department of Mineralogy, Petrology, and Geochemistry, Faculty of Geology, Geophysics and Environmental Protection, AGH-UST in Kraków, Poland.

Table 1

Location, description and mineralogy of major ore types.

Type	Samples	Locality	GPS coordinates		Description	Mt	Hm	Ap	Mnz	Xn	Zrn	Ilm	Ms	Bt	Qtz	Chl
1	MAG-1	S Laurantzonfjellet	N78°44′6.0′′	E10°57′5.4′′	Brecciated Mt-dominated ore	xxx	x	xxx	x	x	x	x	x	x	xx	x
2	MM-18:1a&b	W Boureefjellet	N78°42′35.6″	E10°55′20.3″	Banded Hm-Mt ore with Ms-Ab-Qtz and Ap laminas	xx	xxx	xxx	xx		x		xx		xx	xx
3	MAG-2	SW Boureefjellet pillar	N78°42′26.6′′	E10°55′24.3′′	Augen- gneiss like Mt-Hm ore	xx	xx	xx	x	x	x		xx		xx	xx
4	MAG-3	Bourefjellet ridge	N78°42′52.6′′	E10°57′32.1′′	Skeletal Hm in Qtz + Ap vein	x	xx	x	x/-	x					xxx	xx

Mineral abbreviations hereandafter: Mt – magnetite, Hm – hematite, Ilm – ilmenite, Qtz – quartz, Ap – apatite, Bt – biotite, Chl – chlorite, Ms – muscovite, Mnz – monazite, Xn – xenotime, Zrn – zircon, Ab – albite.

xxx – abundant, xx – common, x – rare, x/- – exceptional.

3.2. Scanning electron microscopy (SEM) and electron probe micro analysis (EPMA)

Back-scatter electron imaging (BSE) and determination of iron oxide, phosphate, and silicate mineral chemistry via wavelength-dispersive spectrometry (WDS) were performed on a JEOL JXA 8530FE electron probe microanalyzer (EPMA) at the Earth Sciences Institute of Slovak Academy of Sciences in Banská Bystrica (SAV BB), Slovak Republic. Additionally, a set of monazite analysis was acquired on a Cameca SX-100 EPMA, at the Department of Microanalysis at Dionýz Štúr State Geological Institute, Geological Survey of Slovak Republic in Bratislava, Slovak Republic (GUDŠ). Uncertainty in the WDS measurements is estimated to be around 3σ.

Iron oxides were analysed using a 20 kV accelerating voltage, a 20nA beam current, and a 1–5 μm beam diameter. Counting times were 20–10 s on peak and 10–5 s on background. Reference standards used were (detection limits in ppm in brackets): Ca(Kα) – diopside (80), Mn(Kα) – rhodonite(140), V(Kα) – ScVO$_4$ (176), Mg(Kα) – diopside (67), Si(Kα) – orthoclase (111), Al(Kα) – albite (82), Zn(Kα) – gahnite (346), Ni(Kα) – nickel silicide (320), Cr(Kα) – Cr$_2$O$_3$ (153), Fe(Kα) – hematite (433), and Ti(Kα) – rutile (606). EPMA analyses for magnetite and hematite are found in Table 2.

Phosphates were analysed in SAV BB using a 15 kV accelerating voltage and a beam current of 20nA. Counting times for Th, U, and Pb were 30 s on peak and 15 s on background, and for REE 20 s on peak and 10 s on background. The beam diameter varied from 2 to 7 μm depending on the grain size. EPMA data was reduced using the ZAF correction method. Standards for the REE-bearing minerals (apatite, monazite, and xenotime) included: Ca(Kα) – diopside, apatite, F(Kα) – fluorite, Cl(Kα)- Tugtupite, Na(Kα) – albite, Sr(Lα) – celestite, Si(Kα, TAP) – albite, Al(Kα) – albite, Mg(Kα) – diopside, K(Kα) – orthoclase, P (Kα) (for apatite) – apatite, U(Mβ) – UO$_2$, Th(Mα) – thorianite, Pb(Mβ) – crocoite, Y(Lα) – YPO$_4$, Lu(Lα) – LuPO$_4$, Ho(Lβ) – HoPO$_4$, Yb(Lα) –

YbPO$_4$, Tm(Lα) – TmPO$_4$, Er(Lα) – ErPO$_4$, Gd(Lβ) – GdPO$_4$, Dy(Lα) – DyPO$_4$, Tb(Lα) – TbPO$_4$, Sm(Lβ) – SmPO$_4$, Eu(Lα, LIFH) – EuPO$_4$, Pr(Lβ) – PrPO$_4$, Nd(Lα) – NdPO$_4$, P(Kα) (for monazite) and Ce(Lα) – CePO$_4$, La (Lα) – LaPO$_4$, Hf(Mα) – cubic zirconia, Zr(Lα) – cubic zirconia, Fe(Kα) – hematite, Mn(Kα) – rhodonite, Cr(Kα) – Cr$_2$O$_3$, V(Kα) – vanadinite, Ti (Kα) – rutile, Ba(Lα) – barite, Sc(Kα) – ScVO$_4$, and S(Kα) – barite. Line interference corrections were Nd → Ce, Eu → Nd, Pr, Gd → Ho, Tm → Sm, Nd → Ce Lu → Dy, Lu → Ho, U → Th, K, and V → Ti (cf. Åmli and Griffin, 1975). Analytical conditions of analysis of monazite in GUDŠ were as follows: 15 kV accelerating voltage, 180 nA beam current, and 1–3 μm beam diameter. Counting times were as follows: Pb – 300 s for its peak position and 2x150 s for background, Th – 35 s for peak and 2 × 17.5 s for background, U – 80 s for peak and 80 s for background, Y – 40 s for peak and 2x20 s for background. The following standards were used in the analytical calibration: Pb(Mα) – PbCO$_3$, Th (Mα) – ThO$_2$, U(Mβ) – UO$_2$, La(Lα) – LaPO$_4$, Ce(Lα) – CePO$_4$, Pr(Lβ) -PrPO$_4$, Nd(Lα) – NdPO$_4$, Sm(Lα) – SmPO$_4$, Eu(Lβ) – EuPO$_4$, Gd(Lα) – GdPO$_4$, Tb(Lα) – TbPO$_4$, Dy (Lβ) – DyPO$_4$, Ho(Lβ) – HoPO$_4$, Er(Lβ) – ErPO$_4$, Tm(Lα) – TmPO$_4$, Yb(Lα) -YbPO$_4$, Lu(Lβ) -LuPO$_4$, K(Kα) – orthoclase, S(Kα) – barite, Ca(Kα) – wollastonite, Sr(Lα) -SrTiO$_3$, Al(Kα) – Al$_2$O$_3$, Si(Lα) – wollastonite, and Fe – fayalite. EPMA analyses for apatite, and monazite and xenotime are found in Tables 3 and 4, and Appendices 2 and 3, respectively. Detection limits for apatite are found in Appendix 2 and for monazite and xenotime in Appendix 3.

Silicate minerals were analysed using a 15.0 kV accelerating voltage and 17nA beam current. Representative EPMA analyses for biotite, muscovite, chlorite, and albite are found in Table 5. Ca(Kα) – diopside, K (Kα) – orthoclase, Na(Kα) – albite, Mn(Kα) – rhodonite, Mg(Kα) (albite) – diopside, Mg(Kα) (micas and chlorite) – biotite, Si(Kα) (micas and chlorite) – biotite, Si(Kα) (albite) – orthoclase, Al(Kα) (micas) – orthoclase, Al(Kα) (albite) – albite, Zn(Kα) – gahnite, Ni(Kα) – nickel silicide, Cr(Kα) – Cr$_2$O$_3$, Fe(Kα) – hematite, P(Kα) – apatite Sr (Lα) – celestite, Ba (Lα) – barite, Cl (Kα) – tugtupite, F(Kα) – fluorite, and Ti(Kα) – rutile.

Table 2

Oxide mineral EMP analysis.

Ore type	comment	analysis no	SiO$_2$	TiO$_2$	Al$_2$O$_3$	Cr$_2$O$_3$	V$_2$O$_3$	Fe$_2$O$_3$*	FeO *	MnO	ZnO	MgO	CaO	NiO	Total
Type (1)	angular Mt	MAG-1 mt 2	0.50	0.01	0.22	0.11	0.41	67.70	31.81	0.01		0.01	0.03	0.03	100.81
Type (1)	centre of Mt crystal	MAG-1 mt 8	0.63	0.03	0.13	0.11	0.34	65.83	31.28	0.02	0.05				98.44
Type (1)	rim of Mt crystal	MAG-1 mt 9	0.03	0.00	0.03	0.02	0.39	67.16	30.38	0.02	0.00				98.07
Type (2)	Hm lepidoblast	MM18 mt 3	0.40	0.01	0.08	0.04	0.42	97.29	1.03	0.01	0.02		0.01	0.03	99.33
Type (2)	Mt porphyroblast	mt18 mt6	0.03	0.00	0.01	0.11	0.39	68.78	31.13			0.00		0.04	100.50
Type (2)	Mt porphyroblast	mt18 mt21	0.31	0.05	0.04	0.08	0.40	68.26	31.66						100.79
Type (3)	porphyroblast of Mt	MAG-2 mt 10	0.26	0.01	0.05	0.09	0.39	68.64	31.56	0.01	nd	0.01	0.01	0.03	101.05
Type (3)	inclusion-rich Mt porphyroblast rim	MAG-2 mt 6	0.05	0.05	0.02	0.41	0.39	67.57	30.80				0.01		99.30
Type (3)	Hm lepidoblast	MAG-2 mt 8	0.04	0.23	0.11	0.03	0.27	96.94	0.59	0.01			0.02		98.24
Type (4)	dendritic Hm	MAG-3 mt 2	0.01	0.59	0.09	0.03	0.50	97.73	1.24	0.00		nd	0.01		100.19
Type (4)	relict Mt within Hm	MAG-3 mt 5	0.02	0.02	0.03	0.01	0.27	69.12	31.21	0.00	0.02			0.03	100.73
Type (4)	Hm veinlet in Ap	MAG-3b mt 1	0.01	0.41	0.08	0.02	0.37	96.95	0.85	0.00	0.01		0.01		98.71

* FeO and Fe$_2$O$_3$ estimated after Droop (1987) on the basis of 2 cations and 3 oxygens (Hm) and 3 cations and 4 oxygens (Mt). nd – not determined; blank – below the EPMA detection limit.

Table 3
Representative apatite EMP analysis.

Ore type	Comment	# pts	P₂O₅	SiO₂	SO₃	Y₂O₃	La₂O₃	Ce₂O₃	Pr₂O₃	Nd₂O₃	Sm₂O₃	CaO	SrO	BaO	FeO	MnO	Na₂O	F	Cl	H₂O	Sum	F=O	Cl=O	Total	(REE+Y)₂O₃	P	Si	S	Y	La	Ce	Pr	Nd	Sm	Ca	Sr	Ba	Mn	Fe	Na	F	Cl	OH*	X_Fap	X_Sap	X_OHap
Type (1)	subhedral Ap within Chl vein		42.56	0.07	0.01	0.03		0.09		0.07	0.03	55.14	0.15		0.26	0.09	0.04	3.41	0.30	0.21	102.52	1.44	0.07	101.01	0.22	5.99	0.01	0.00	0.00		0.01		0.00	0.00	9.83	0.01		0.01	0.04	0.01	1.79	0.08	0.12	0.90	0.04	0.06
Type (1)	inclusion in Mt		42.83	0.02	0.01			0.03	0.02	0.05	0.02	55.29	0.14	0.03	0.90	0.03		2.75	0.92	0.57	103.76	1.16	0.21	102.40	0.12	5.97	0.00	0.00			0.00	0.00	0.00	0.00	9.75	0.01	0.00	0.03	0.12		1.43	0.26	0.31	0.71	0.13	0.16
Type (1)	Ap hosting Mnz		41.33	0.30		0.06	0.06	0.24		0.15		55.35	0.00		0.30		0.08	2.89	0.25	0.72	102.00	1.22	0.06	100.73	0.63	5.85	0.05		0.01	0.00	0.01		0.00		9.91	0.00		0.07	0.04	0.07	1.53	0.07	0.40	0.76	0.03	0.20
Type (1)	interstitial between Mt-core		42.27	0.03	0.01	0.08	0.04	0.10	0.00	0.03	0.00	54.99	0.00	0.00	0.12	0.02	0.02	2.99	0.37	0.56	100.42	1.26	0.08	100.42	0.25	5.97	0.01	0.01	0.01	0.01	0.01	0.00	0.00	0.00	9.83	0.00	0.00	0.01	0.02	0.01	1.58	0.10	0.31	0.79	0.05	0.16
Type (1)	interstitial between Mt-rim		42.31	0.03	0.01	0.05	0.03	0.07	0.05	0.09	0.00	55.06	0.01	0.17	0.08	0.02	0.01	3.20	0.39	0.36	100.65	1.35	0.09	100.65	0.33	5.98	0.01	0.01	0.01	0.00	0.01	0.00	0.01	0.00	9.85	0.00	0.01	0.01	0.02	0.01	1.69	0.11	0.20	0.84	0.05	0.10
Type (2)	Ap nest		43.35	0.03		0.03	0.00	0.15	0.05	0.48		55.68	0.11		0.37		0.01	2.57	0.46	1.02	103.68	1.08	0.10	102.50	0.06	5.97	0.01		0.00	0.00	0.01	0.00	0.03		9.71	0.01		0.04		0.00	1.32	0.13	0.55	0.66	0.06	0.28
Type (2)	Ap nest		42.55	0.03		0.05	0.02	0.04	0.00	0.20	0.00	55.50	0.10		0.44			2.76	0.51	0.75	103.77	1.16	0.11	101.50	0.12	5.95	0.00		0.00	0.00	0.00	0.00	0.01	0.00	9.82	0.01		0.06			1.44	0.14	0.41	0.72	0.07	0.21
Type (2)	Ap intergrown with mt and Hm - darker core		41.88	0.21	0.01	0.06	0.02	0.00	0.00	0.03	0.01	55.48	0.04	0.19	0.05	0.00	0.02	2.61	0.52	0.86	101.94	1.10	0.12	100.73	0.13	5.91	0.00	0.00	0.00	0.00	0.00	0.00	0.00	0.00	9.91	0.00	0.01	0.01	0.00	0.01	1.38	0.15	0.48	0.69	0.07	0.24
Type (2)	Ap intergrown with mt and Hm - brighter rim		42.30	0.07	0.01	0.07	0.05	0.00	0.03	0.09		55.60	0.00	0.11	0.52	0.11	0.01	2.76	0.39	0.82	102.82	1.16	0.09	101.57	0.18	5.92	0.01	0.01	0.01	0.00	0.00	0.00	0.00		9.84	0.00	0.01	0.07	0.00	0.00	1.44	0.11	0.45	0.72	0.06	0.23
Type (3)	intergrown with Hm in Qtz veinlet		42.41	0.01		0.12	0.02	0.08	0.06	0.05	0.03	53.29	0.86		0.35	0.30	0.04	1.69	2.19	0.88	102.39	0.71	0.49	100.19	0.38	6.00	0.00		0.01	0.00	0.00	0.00	0.00	0.00	9.54	0.08		0.04	0.04	0.01	0.89	0.62	0.49	0.45	0.31	0.24
Type (3)	in Chl lamina		42.32	0.07		0.02	0.00	0.03	0.08	0.05	nd	54.52			0.56	0.28	0.04	1.90	1.56	1.04	102.94	0.80	0.35	100.79	0.25	5.93	0.01		0.00	0.00	0.00	0.00	0.00		9.67	0.04		0.04	0.04	0.01	0.99	0.44	0.57	0.33	0.22	0.29
Type (3)	Porphyroblast between Hm-Bright areas (Fig.4D)		40.43			0.14	0.02	0.08	0.08	0.08	0.03	50.71	1.05		0.97	1.21	0.06	1.20	2.69	0.96	99.66	0.51	0.61	98.55	0.36	5.93			0.14	0.00	0.01	0.01	0.01	0.00	9.41	0.11		0.14	0.18	0.02	0.66	0.79	0.55	0.33	0.39	0.28
Type (3)	Porphyroblast between Hm-dark areas (Fig.4D)		41.83			0.08	0.03	0.13	0.01	0.08	0.02	54.09	0.25	0.06	0.30	0.14	0.07	1.52	2.31	0.52	102.11	1.00	0.52	100.96	0.18	5.95			0.04	0.01	0.01	0.00	0.01	0.00	9.74	0.02	0.00	0.04	0.04	0.02	0.81	0.66	0.54	0.44	0.33	0.27
Type (3)	Ap intergrown with Ms, Qtz and Hm		41.30	0.01		0.04	0.00	0.00	0.01	0.06	0.02	53.26	0.00	0.19	0.58	0.16	0.07	1.15	3.09	0.87	100.27	0.48	0.69	100.36	0.28	5.93	0.00		0.01	0.00	0.00	0.00	0.01	0.00	9.68	0.00	0.01	0.08	0.02	0.02	0.62	0.89	0.49	0.31	0.44	0.25
Type (4)	massive Ap in Qtz vein-core		42.06	0.01		0.05		0.05		0.03	0.03	51.63	0.84	0.30	1.19	0.89	0.05	1.71	1.93	0.96	101.69	0.72	0.43	100.54	0.13	6.00	0.00		0.01		0.01		0.00	0.00	9.32	0.08	0.02	0.13	0.16	0.02	0.91	0.55	0.54	0.46	0.28	0.27
Type (4)	massive Ap in Qtz vein-rim		41.86	0.03		0.08	0.02	0.03	0.04		0.00	56.58	1.04	0.35	1.33	1.13	0.02	1.25	2.58	1.04	99.93	0.53	0.58	99.93	0.19	6.01	0.00		0.01	0.00	0.00	0.00		0.00	9.19	0.10	0.02	0.16	0.19	0.02	0.67	0.74	0.59	0.34	0.37	0.29
Type (4)	intergrown with Hm and Qtz		41.66	0.03		0.05	0.03	0.01	0.00	0.01	0.00	55.16	0.63	0.18	1.08	1.06	0.06	1.50	2.30	0.52	100.75	0.63	0.52	100.73	0.10	6.00	0.00		0.01	0.00	0.00	0.00	0.00	0.00	9.32	0.06	0.01	0.15	0.15	0.02	0.81	0.66	0.53	0.40	0.33	0.27
Type (4)	Ap vein in Qtz		41.30	0.01		0.07	0.05	0.00	0.05	0.06	0.01	55.13	0.98		1.11	1.14	0.06	1.48	2.34	0.94	101.00	0.62	0.53	99.85	0.20	5.95	0.00		0.01	0.01	0.00	0.00	0.00	0.00	9.49	0.07		0.14	0.16	0.02	0.86	0.65	0.49	0.40	0.34	0.27

blank – element was below the EPMA detection limit; * – OH calculated per charge balaance on the halogen site for a total of 2 anions.

Table 4
Representative monazite and xenotime EMP analyses.

Ore Type	Comment	Mineral	P₂O₅	As₂O₅	ThO₂	UO₂	SiO₂	SO₃	Y₂O₃	La₂O₃	Ce₂O₃	Pr₂O₃	Nd₂O₃	Sm₂O₃	Eu₂O₃	Gd₂O₃	Tb₂O₃	Dy₂O₃	Ho₂O₃	Er₂O₃	Tm₂O₃	Yb₂O₃	Lu₂O₃	CaO	PbO	SrO	FeO	H₂O	Sum	F=O	Cl	Total	P	As	Th	U	Si	S	Y	La	Ce	Pr	Nd	Sm	Eu	Gd	Tb	Dy	Ho	Er	Tm	Yb	Lu	Ca	Fe	Pb	Sr
Type 1	inclusion in Ap	Mnz	31.33	0.08	0.81	0.50	0.10	0.13	0.65	13.75	30.16	3.48	14.33	1.19	0.33	1.31	0.08	0.17	0.00	0.00	0.008	0.02	0.19	1.18	nd	0.60			100.55			100.55	3.909	0.006	0.054	0.017	0.030	0.010	0.051	0.748	1.627	0.183	0.770	0.060	0.055	0.064	0.004	0.008	0.000	0.000	0.008	0.001	0.009	0.052		0.000	0.012
Type 1	inclusion in Mt	Mnz	29.21		3.27	0.33	0.08	0.02	0.55	10.75	31.31	3.06	15.71	1.29	0.52	1.41	0.00				0.003	0.09		0.72					100.91			99.58	3.830		0.230	0.036	0.025	0.009	0.045	0.603	1.757	0.224	0.886	0.095	0.081	0.092	0.000	0.000		0.001	0.003	0.000	0.004	0.081		0.003	0.000
Type 1	inclusion in Mt	Mnz	29.84	0.07	1.95	0.28	0.30	0.05	0.50	10.55	30.92	3.37	14.94	2.12	0.41	1.23	0.00				0.010	0.03		0.64					99.52			99.52	3.911	0.005	0.137	0.024	0.002	0.007	0.045	0.703	1.768	0.186	0.702	0.117	0.063	0.067	0.000			0.000	0.007	0.001	0.000	0.096		0.007	0.000
Type 1	inclusion in Mt	Mnz	29.83	0.10	1.17	0.40	0.03	0.13	0.67	13.22	29.56	3.71	14.86	2.89	0.49	1.52	0.00	0.21			0.002	0.08		0.63					99.46			99.46	3.888	0.008	0.082	0.014	0.003	0.009	0.055	0.752	1.670	0.204	0.836	0.153	0.054	0.085	0.000	0.011		0.001	0.002	0.000	0.009	0.054		0.002	0.000
Type 1	inclusion in Mt	Xn	35.09	0.03	0.03	0.31	0.00	0.00	44.11	0.15	0.48	0.05	0.48	0.70	0.16	2.48	1.31	4.37	0.56	0.52	0.168	3.19	3.91	0.45					99.74			99.74	3.937	0.003	0.016	0.023	0.042	0.000	3.051	0.003	0.007	0.003	0.011	0.024	0.016	0.124	0.050	0.268	0.023	0.023	0.023	0.174	0.168	0.052	0.223		0.017	0.020
Type 1	interstitial	Xn	34.31	0.00	0.38	0.27	0.15	0.02	42.29	0.05	0.04	0.00	0.21	0.52	0.00	2.77	1.16	6.13	1.15	0.64	0.164	4.22	3.96	0.53					100.32			100.32	3.961	0.000	0.019	0.018	0.009	0.002	3.129	0.003	0.030	0.000	0.023	0.032	0.056	0.269	0.056	0.313	0.047	0.030	0.019	0.130	0.164	0.071	0.224		0.007	0.000
Type 1	interstitial	Xn	34.49	0.21	0.38	0.19	0.00	0.00	41.87	0.01	0.06	0.00	0.20	0.49	0.00	2.78	1.28	6.65	1.10	0.76	0.176	4.35	4.14	0.53					99.04			99.04	3.946	0.015	0.019	0.012	0.026	0.001	3.011	0.000	0.027	0.000	0.034	0.023	0.055	0.290	0.063	0.365	0.052	0.039	0.016	0.176	0.176	0.080	0.165		0.025	0.000
Type 1	intergrown with Ms	Xn	36.35	0.15	0.10	0.11	0.01	0.01	41.53	0.01	0.01	0.00	0.17	0.28	0.28	3.45	1.20	6.16	1.26	0.89	0.173	4.14	4.26	0.16					99.67			99.67	3.962	0.010	0.005	0.006	0.001	0.001	2.860	0.000	0.001	0.000	0.008	0.013	0.026	0.139	0.049	0.326	0.006	0.049	0.013	0.163	0.173	0.466	0.013		0.002	0.000
Type 2	intergrown with Ms and Ms.	Mnz	30.58	0.04	0.84	0.05	0.11	0.01	0.53	13.85	31.65	3.63	14.08	1.19	0.79	1.52	0.00	0.00	0.004		0.009	0.25	0.21	0.95			0.07		100.95		0.07	100.95	3.926	0.003	0.058	0.003	0.022	0.025	0.043	0.775	1.757	0.197	0.778	0.128	0.052	0.086	0.000	0.000	0.004		0.009	0.052	0.052	0.081		0.004	0.000
Type 2	inclusion in Ab	Mnz	29.45	0.00	3.84	0.04	0.08	0.07	0.70	12.73	29.20	3.30	12.74	2.98	0.69	1.40	0.00	0.07	0.017		0.005	0.02	0.02	0.71			0.07		99.78		0.04	99.78	3.731	0.000	0.261	0.003	0.006	0.018	0.056	0.703	1.600	0.176	0.694	0.126	0.074	0.056	0.000	0.004	0.017		0.007	0.007	0.172	0.052		0.001	0.012
Type 2	overgrowth on Ap in Ab-Qtz domain	Mnz	29.58	0.66	1.50	0.03	0.59	0.08	0.67	12.73	31.67	3.41	12.63	2.12	0.04	1.33	0.00	0.15	0.020		0.004	0.00	0.02	0.64			0.08		100.75		0.01	100.75	3.819	0.036	0.104	0.002	0.046	0.029	0.054	0.864	1.768	0.186	0.682	0.117	0.000	0.063	0.000	0.008	0.020		0.004	0.001	0.096	0.268		0.004	0.007
Type 2	intergrown with Chl	Mnz	30.48	0.11	2.52	0.07	0.23	0.12	0.54	14.63	30.97	2.88	12.65	1.85	0.00	1.22	0.00	0.00	0.007		0.002	0.00	0.05	0.58			0.05		100.64		0.05	100.64	3.832	0.009	0.170	0.004	0.069	0.042	0.042	0.801	1.684	0.153	0.685	0.095	0.000	0.060	0.000	0.000	0.007		0.002	0.000	0.184	0.069		0.002	0.004
Type 3	Mnz intergrown with silicates	Mnz	31.05		5.56	0.20	0.21	0.13	0.65	14.24	28.93	3.04	11.98	0.81	0.38	1.31	0.05	0.00	0.000		0.12	0.07	0.80	1.21			0.93		102.18		0.12	102.18	3.796		0.362	0.016	0.027	0.025	0.049	0.759	1.513	0.155	0.623	0.049	0.038	0.034	0.009	0.000	0.000		0.003	0.081	0.062	0.117	0.223		0.045	0.020
Type 3	Mnz intergrown with silicates	Mnz	30.36		5.52	0.33	0.08	0.02	0.50	10.75	31.83	3.05	12.61	0.82	0.34	0.92	0.01	0.08	0.000		0.15	0.03	0.61	0.72		nd	0.62		99.58		nd	99.65	3.830		0.362	0.015	0.062	0.004	0.040	0.952	1.757	0.164	0.693	0.081	0.040	0.057	0.002	0.020	0.000		0.004	0.009	0.072	0.016	0.224		0.047	0.003
Type 3	Fig. 6d brighter area	Mnz	31.01		5.75	0.45	0.12	0.11	1.07	16.07	28.86	3.09	10.86	0.88	0.16	0.83	0.04	0.08	0.004		0.08	0.04	0.43	1.48		nd	0.69		101.86		nd	101.87	3.757		0.362	0.022	0.016	0.022	0.081	0.848	1.512	0.155	0.586	0.051	0.016	0.039	0.004	0.020	0.004		0.002	0.001	0.165	0.047	0.455		0.045	0.017
Type 3	Fig. 6d brighter area	Mnz	30.61	0.11	3.77	0.30	0.12	0.42	0.72	15.80	30.72	3.09	10.67	0.95	0.32	0.84	0.06	0.09	0.019		0.19	0.04	0.22	1.70		0.58	0.84		101.87	0.01	0.58	101.87	3.635	0.011	0.241	0.019	0.019	0.050	0.053	0.817	1.577	0.155	0.555	0.042	0.032	0.040	0.006	0.004	0.019		0.008	0.003	0.196	0.176	0.511		0.001	0.017
Type 3	interstitial between Hm and Hm	Mnz	30.26	0.00	3.09	0.31	0.07	0.72	0.91	13.21	29.36	3.81	16.67	2.68	0.32	3.26	0.12	0.22			0.17	0.19	0.60	0.41		0.01	0.17		100.27		0.01	100.27	3.809	0.000	0.197	0.041	0.050	0.202	0.072	0.724	1.598	0.202	0.685	0.137	0.026	0.137	0.032	0.051			0.077	0.032	0.049	0.013	0.271		0.001	0.029
Type 3	intergrown with Hm	Xn	33.86	0.14	0.00	0.17	0.19	0.13	40.87	0.00	0.00	0.00	0.00	0.29	0.18	4.27	1.04	4.37	0.56	0.44	0.135	3.44	3.63	0.45			2.57		98.97		2.57	98.97	3.685	0.010	0.000	0.009	0.050	0.029	0.147	0.000	0.000	0.000	0.002	0.013	0.181	0.227	0.023	0.181	0.023	0.147	0.135	0.552	0.058	0.223	0.370		0.000	0.000
Type 3	intergrown with Hm	Xn	36.87	0.14	0.00	0.11	0.19	0.03	42.41	0.00	0.00	0.00	0.05	0.33	0.00	3.18	0.42	2.90	1.15	0.51	0.047	4.22	3.73	0.53			1.51		99.65		1.51	99.65	4.024	0.010	0.000	0.006	0.015	0.012	2.909	0.000	0.000	0.000	0.003	0.018	0.042	0.227	0.037	0.181	0.047	0.021	0.071	0.325	0.071	0.051	0.154		0.000	0.000
Type 3	intergrown with Hm	Xn	36.84	0.09	0.00	0.05	0.05	0.03	41.33	nd	0.00	0.00	0.02	0.24	0.23	3.18	0.53	3.03	1.10	0.47	0.149	3.77	4.03	2.04			1.11		99.32		1.11	99.32	4.046	0.006	0.000	0.002	0.017	0.003	2.853		0.000	0.000	0.001	0.031	0.031	0.148	0.045	0.164	0.045	0.019	0.080	0.240	0.025	0.126	0.008		0.000	0.025
Type 3	inclusion in Ap	Xn	36.60	0.06	0.02	0.30	nd	0.02	43.02	0.00	0.06	0.06	nd	0.31	0.07	2.78	0.00	1.60	0.95	0.03		3.90	4.01	1.26			1.60		99.79		1.60	99.79	4.081	0.004	0.000	0.017		0.004	2.956	0.000	0.003	0.003		0.015	0.004	0.116	0.000	0.055	0.039	0.160		0.039	0.043	0.272	0.000		0.014	0.043
Type 4	Retiel Mnz in Hm	Mnz	28.55		5.48	0.32	0.76	0.02	3.22	13.13	26.83	2.83	11.58	1.83		1.87		0.19				0.15	0.17	0.67					98.80			98.80	3.667		0.378	0.011	0.206	0.000	0.260	0.735	1.490	0.153	0.640	0.096		0.094		0.009				0.009	0.007	0.014	0.217		0.000	0.000
Type 4	Ap rim grain	Xn	36.27	0.10	0.07	1.11	0.02	0.00	45.01	0.01	0.04	0.00	0.07	0.22	0.03	3.33	0.43	4.63	0.42	0.42	0.020	1.53	1.96	0.56			0.50		102.58		0.50	102.58	3.925	0.007	0.004	0.063	0.002	0.000	3.062	0.001	0.002	0.000	0.004	0.012	0.001	0.141	0.018	0.191	0.017	0.017	0.022	0.155	0.107	0.154	0.000		0.000	0.000
Type 4	Ap rim grain	Xn	36.79	0.11	0.03	0.92	0.01	0.00	41.12	0.00	0.00	0.00	0.04	0.17	0.03	2.93	0.59	3.15	0.59	0.53	0.016	3.55	1.83	0.43			1.18		100.59		1.18	100.59	3.809	0.007	0.002	0.050	0.001	0.000	2.676	0.000	0.000	0.000	0.002	0.008	0.001	0.119	0.026	0.124	0.023	0.023	0.016	0.242	0.047	0.242	1.145		0.000	0.000
Type 4	inclusion in Ap	Xn	36.86		0.08	0.86	0.00	0.13	38.01	0.01	0.00	0.03	0.00	0.16	0.16	3.44	0.24	4.62	0.68	0.46	0.015	3.03	1.28	0.46			0.02		100.08		0.02	100.08	3.761		0.004	0.046	0.000	0.031	2.438	0.001	0.000	0.001	0.000	0.009	0.179	0.131	0.089	0.137	0.111	0.046	0.015	0.111	0.046	1.737	0.000		0.014	0.000

blank – element was below the EPMA detection limit.

Table 5
Silicate mineral EMP analysis.

Ore type	Mineral	SiO_2	TiO_2	Al_2O_3	Cr_2O_3	FeO	MnO	MgO	CaO	Na_2O	K_2O	P_2O_5	BaO	SrO	F	Cl	H_2O^*	Total
type (1)	Bt	35.30	1.47	15.25	0.06	25.71	0.07	6.61	0.02	0.05	8.82	0.00	0.66			2.37	3.14	99.52
type(1)	Bt	35.10	1.78	16.08	0.03	25.73		6.30	0.04	0.06	8.17	0.00	0.31			1.73	3.74	99.06
type (3)	phengitic Ms	50.56	0.09	32.10		5.22	0.01	1.03	0.02	0.17	10.45	0.02	0.13			0.01	4.65	104.46
type(2)	phengitic Ms	48.59	0.01	35.08		2.80		0.28	0.03	0.91	8.57		0.39	0.03		0.01	4.57	101.26
type (2)	Ms	47.80	0.07	35.61	0.02	2.11	0.04	0.27	0.01	1.84	8.65	0.01	0.24			0.01	4.59	101.23
type (2)	Ms	47.58	0.09	35.83	0.02	1.98	0.02	0.18	0.01	1.68	8.80	0.02	0.24	0.01		0.01	4.56	101.03
type (1)	Chl	26.32	0.06	20.58	0.05	27.19	0.08	14.22	0.22	0.05	0.03	0.02				0.04		88.85
type (1)	Chl	26.06	0.04	20.51		26.23	0.02	14.34	0.21	0.00	0.12	0.11	0.01	0.00	0.07			87.74
type (2)	Ab	67.71	0.06	20.20		0.44	0.05	nd	0.80	11.65	0.09	0.02	0.02	0.11				101.15
type (3)	Ab	67.89	nd	19.86		0.23		0.02	0.60	11.64	0.08	0.01	nd	0.143				100.46

* – estimated from charge balance of F, Cl, and OH on the halogen site.

blank – below the EPMA detection limit.

Detection limits (3σ in ppm) for feldspar are Ca – 60, K – 52, P – 121, Na – 70, Mg – 65, Al – 280, Si – 270, Ba – 190, Sr – 220, Fe – 319, Mn – 336, and Ti – 593. For mica and chlorite, they are Ca – 54, K – 19, P – 750, F – 360, Na – 290, Mg – 255, Al – 219, Si – 100, Ba – 93, Sr – 187, Fe – 300, Mn – 225, and Ti – 350.

4. Ore petrography and mineral chemistry

In outcrop, the IOA ore bodies display four distinct metamorphic and deformational structures and mineral assemblages: breccia Type (1) ore (MAG-1); banded Type (2) ore (MM18-1B); augen Type (3) ore (MAG-2); and Type (4) ore (MAG-3), in which the iron oxides and apatite occurs as dendritic veins in quartz. This diversity is connected to differences in the modal abundances and composition of the iron oxides (magnetite and hematite), phosphates, and silicates, as well as accessory phases (see Table 1). The mineral assemblage in Type (1) ore includes magnetite with minor hematite, ilmenite, apatite, rare monazite and xenotime, and sporadic zircon with a relatively low silicate content (quartz, muscovite, biotite, chlorite, and albite). In Type (2) ore, the modal content of the iron oxides is lower than in Type (1). Hematite is predominant over magnetite. The phosphates are represented by abundant apatite and monazite. Minor zircon is also present. Type (2) ore is characterised by a high silicate content including quartz, muscovite, chlorite, and rare albite. In Type (3) ore, magnetite and hematite occur in equal amounts. Apatite is common, accompanied by rare monazite and xenotime. The silicate mineral assemblage commonly consists of quartz, muscovite, chlorite, and albite. In Type (4) ore, hematite prevails over magnetite. Apatite, xenotime, and monazite occur in limited amounts. Compared to the first three ore types, in Type (4) ore the abundance of iron oxides and phosphates with respect to gangue silicates (abundant quartz and minor sheet silicates) is the lowest. In all four ore types, sulphides are rare, and occur as dispersed pyrite, arsenopyrite, and chalcopyrite inclusions or veinlets in the magnetite.

Magnetite from all four ore types contains similar trace amounts of Ti, Mg, Mn, Ni, Cr, and Al, which rarely exceed 0.20 wt% (Table 2). The V_2O_3 content ranges from 0.20 to 0.50 wt%. The magnetite grains show no textural or compositional zonation. Specular hematite from Types (3) and (4) ore contains trace amounts of Al, Cr, Mg, Ni, and Mn (<0.10 wt %), whereas concentrations of V_2O_3 vary from 0.20 to 0.40 wt% in the hematite, similar to that seen in magnetite. The TiO_2 concentration in hematite can reach up to 0.60 wt%.

4.1. Type (1) ore

Type (1) ore texturally consists of angular grains and aggregates of magnetite and minor hematite, which probably represent cataclased and recrystallised fragments of previously massive magnetite ore, cemented together by a silicate-phosphate matrix (Fig. 3a, b). The arrangement of iron oxide fragments and surrounding phyllosilicates exhibits a very faint parallel orientation. Magnetite strongly predominates (Fig. 3a) and occurs as variably sized (1 mm–10 μm), sub- to euhedral crystals and aggregates (Fig. 3b). The pristine magnetite grains are overgrown by porous, fine-crystalline, possibly reprecipitated magnetite, and rimmed by silicates. Hematite is relatively rare and occurs almost always as lath-like crystals developed along extensional fissures and secondary vein-lets. It also occurs as pseudomorphs after smaller magnetite grains, or as subtle net-like replacements of magnetite along crystallographic planes. Ilmenite is a rare accessory phase, occurring locally as anhedral aggregates intergrown with magnetite.

Apatite distribution within Type (1) ore is random. It mostly forms irregular aggregates of individual small (<100 μm), clustered grains in the interstitial spaces between the magnetite grains (Fig. 4a), as rare inclusions in magnetite, or as accumulations of prismatic crystals (up to 150 μm) within fissures or along the walls of the chlorite-carbonate veinlets as well as within them (Fig. 4b). The boundaries of the apatite aggregates are usually strongly lobate, and locally blurred. Most of the
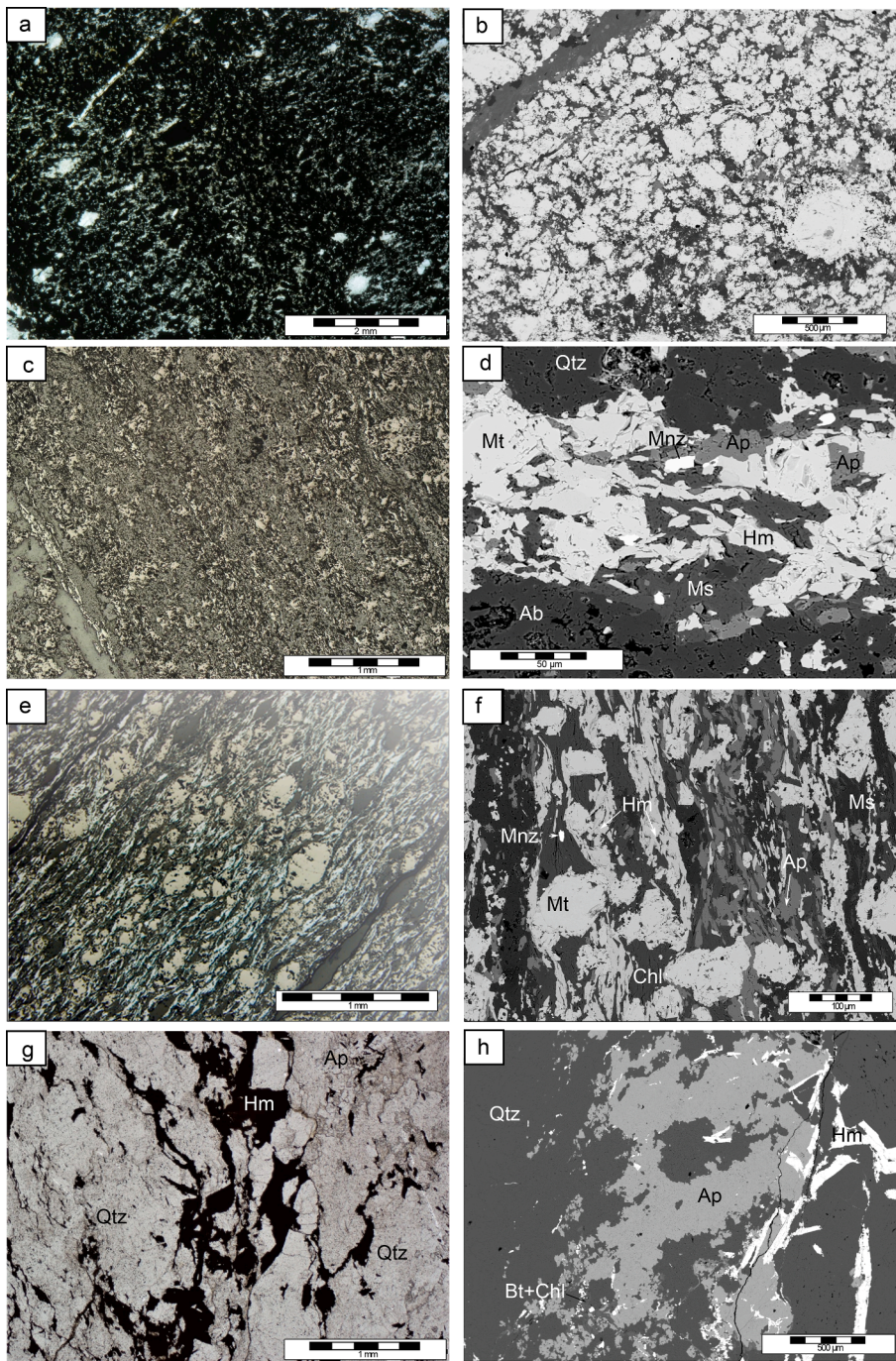
Fig. 3. BSE images and photomicrographs of fabric and assemblages from particular ore types. a) Brecciated Type (1) ore (transmitted light using two polarizers) consisting of magnetite matrix with minor apatite and rare quartz porphyroblasts. Note the apparently massive texture under low magnification. b) Brecciated Type (1) ore (BSE image) with irregular fragments of magnetite (light grey) surrounded by a silicate matrix with irregular apatite aggregates (dark grey). c) Banded Type (2) ore (reflected light using one polarizer) composed of lobate magnetite porphyroblasts and hematite streaks (light gray) alternating with silicate- and apatite-dominated domains (grey). d) Segregation into thin iron oxide, apatite, and quartz-dominated layers in Type (2) ore (BSE image). e) Augen-gneiss ore texture typical of Type (3) ore (reflected light using one polarizer). It is characterized by magnetite porphyroblasts (pinkish) surrounded by aligned lath- and plate-like crystals of hematite and the silicate matrix. f) Magnetite and quartz augen-like porphyroblasts in Type (3) ore (BSE image) associated with lepidoblastic hematite, silicates, and apatite. g) Skeletal Type (3) ore (transmitted light using one polarizer) dominated by dendritic, sheared hematite intergrown with quartz and grainy apatite. h) Dendritic hematite intergrown with apatite within quartz in the skeletal Type (4) ore (BSE image). Mineral abbreviations: Mt – magnetite, Hm – hematite, Qtz – quartz, Ap – apatite, Bt – biotite, Chl – chlorite, Ab – albite, Ms – muscovite, Mnz – monazite, Xn – xenotime.

apatite grains show no textural heterogeneity under BSE imaging. Only in some larger grains is subtle zonation observed, which is manifested by darker and brighter areas. The dark areas are mostly developed along rims or along fissures (Fig. 4e). Of the four ore types, the composition of the apatite in Type (1) ore is closest to that of the ideal fluorapatite endmember (F > 3.12 wt% and X_{F-Ap} > 0.66) with variable admixtures of Cl (Cl < 0.91 wt% and X_{Cl-Ap} < 0.15) and H_2O (X_{OH-Ap} < 0.2; Fig. 5a; Table 3; Appendix 2). MnO, SrO, and BaO contents do not exceed 0.20 wt% (Fig. 5b-d; Table 3), whereas the ThO_2 content is usually < 0.02 wt %. The $(Y + REE)_2O_3$ concentration in the apatite varies from 0.10 to 0.30 and is consistent with low Na and Si contents (Fig. 5e). The highest Y + REE contents are observed only in those apatite grains, which host monazite inclusions (Fig. 6c). In apatite showing textural zonation, the brighter zones are slightly enriched in REE compared to the darker zones.

In Type (1) ore, monazite and xenotime (Fig. 6a and b, respectively) occur as inclusions in magnetite or are intergrown with magnetite and silicates. Monazite inclusions in apatite are rare (Fig. 6c). Monazite forms relatively small (<30 μm), rounded grains. Xenotime grains are slightly larger than monazite (up to 50 μm in diameter). The largest grains exhibit a patchy zoning or the presence of a lighter or darker net of veinlets coupled with a porosity (Fig. 6d). Most of the monazite grains contain 1.20 to 3.50 wt% ThO_2 and variable UO_2 (b.d.l. – 0.50 wt%; Table 4; Appendix 3). Lower abundances of ThO_2 (<1.00 wt%) are typical, especially for monazite inclusions in apatite. Thorium is principally incorporated into monazite via the cheralite-type substitution $(Ca(Th,U)(Y,REE)_{-2})$ (Fig. 7a), but some grains show an excess CaO content of up to 1.2 wt
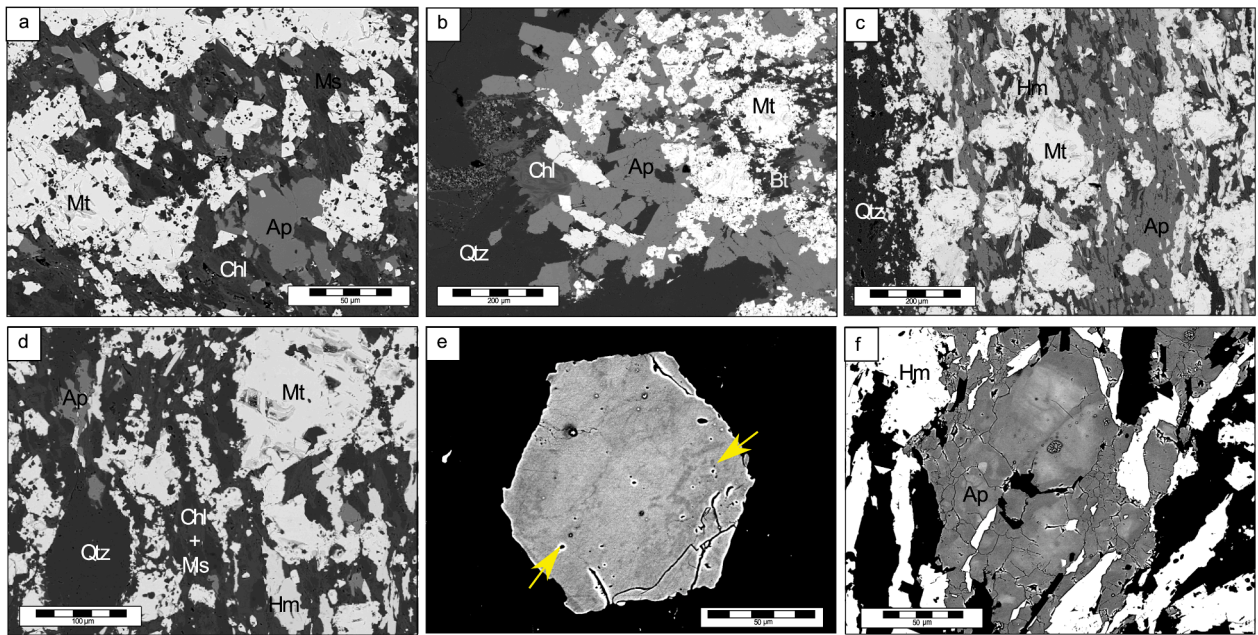
Fig. 4. BSE microphotographs of different modes of the occurrence of apatite within the PKF ores. a) Subhedral apatite crystals within a chlorite matrix in Type (1) ore. Note the irregular grain boundaries. b) Aggregates of lath-shaped, semi euhedral, apatite grains on the wall of an extensional fissure in Type (1) ore. c) Apatite-rich thin layers in Type (2) ore intergrown with magnetite and hematite. d) Small, strongly anhedral, dispersed apatite grains intergrown with magnetite, hematite, and silicate minerals in Type (3) ore. e) Euhedral apatite showing a faint patchy texture. Note the ragged grain boundaries. Yellow arrows point to micropores in apatite, likely due to interaction with fluids. f) Patchy zoned apatite from Type (3) ore. Brighter zones, developed around cracks, have elevated Sr, Mn, and Cl contents with respect to the darker, F-dominated apatite. Mineral abbreviations are given in the Fig. 3 caption.
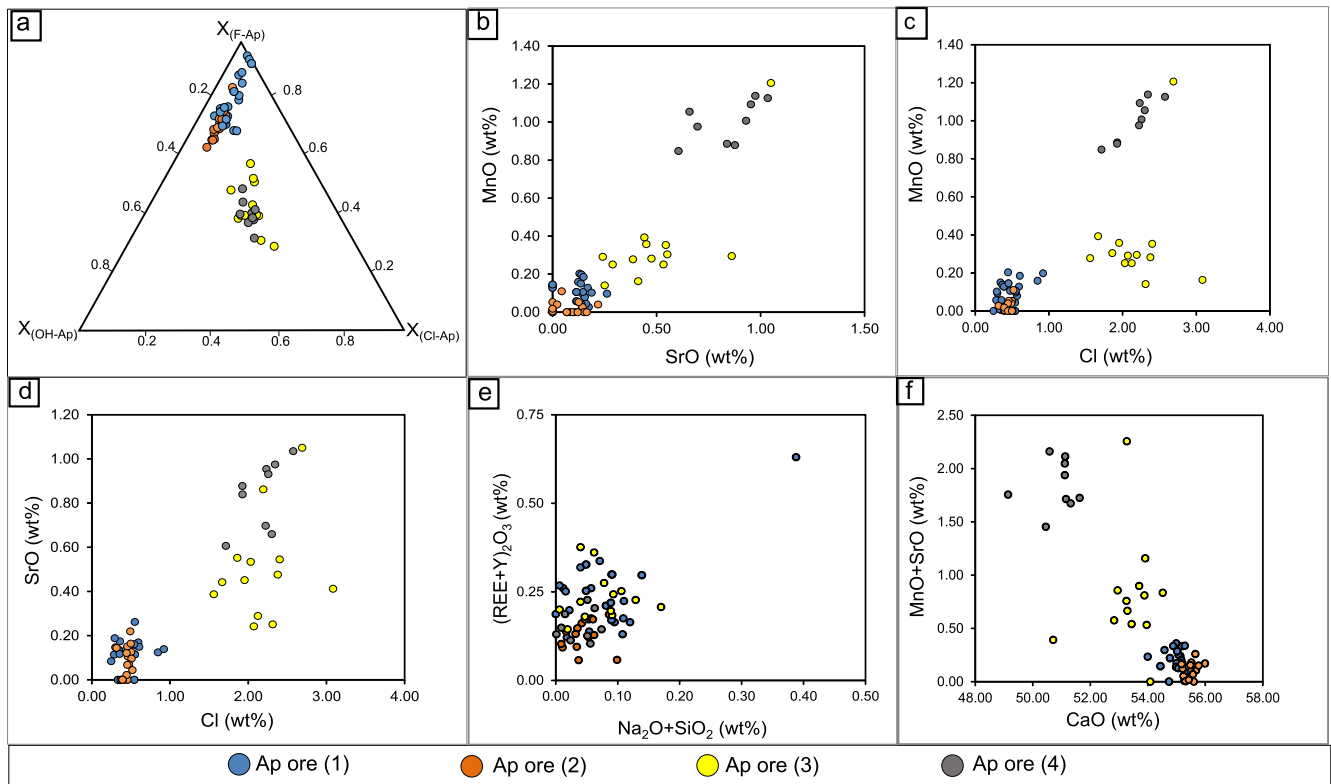
Fig. 5. a) Ternary X_{FAp}-X_{ClAp}-X_{OHAp} diagram showing substitution relations on the halogen site for the PKF apatites from all four ore types. b) Plot of SrO vs. MnO (wt%) for apatite from the PKF IOA ores. c) MnO vs. Cl (wt%) plot for apatite from the PKF IOA ores. d) SrO vs. Cl (wt%) for apatite from the PKF IOA ores. e) Na$_2$O + SiO$_2$ vs. (Y + REE)$_2$O$_3$ for the apatite from the PKF apatite ore bodies, showing a uniform very low REE content in the apatite from all four ore types. f) Negative correlation of CaO vs. MnO + SrO (wt%) in apatite.
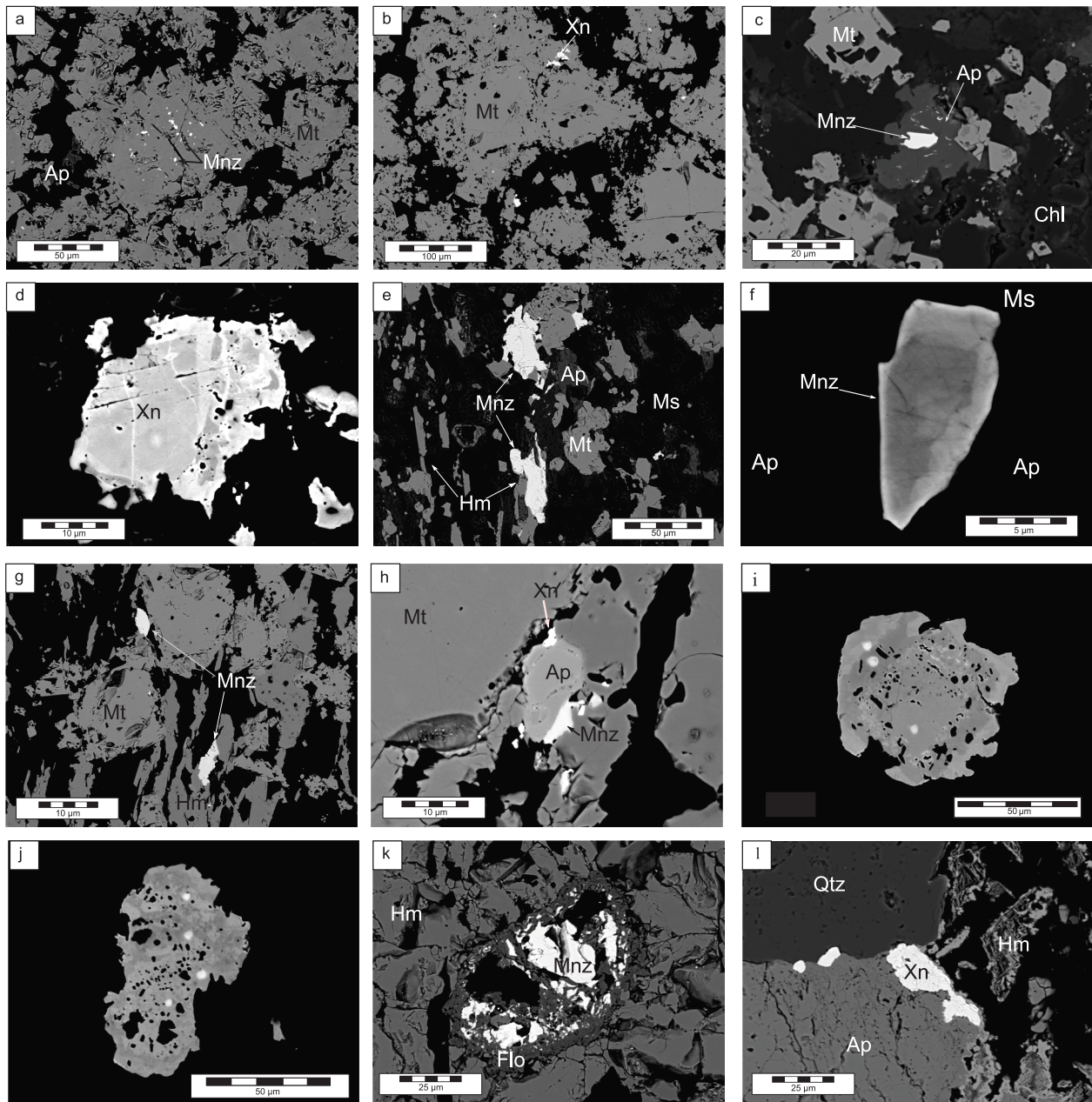
Fig. 6. BSE images of micrographs of the mode of occurrence and textures in monazite and xenotime from the PKF ores. a) Numerous small monazite inclusions (white) enclosed in magnetite (grey) from Type (1) ore. b) Xenotime inclusions in porous magnetite from Type (1) ore. c) Monazite surrounded by a thick rim of anhedral apatite from Type (1) ore. Note the small bright inclusions of monazite in the apatite. d) Xenotime grain with a highly irregular shape. Light patches and stripes correspond to higher U, Th, and LREE domains (brecciated Type (1) ore). e) Large monazite grains intergrown with magnetite and silicates in Type (2) ore. Note the elongation of the monazite grains in a direction parallel to the lineation of the hematite laths. f) Texturally heterogenous monazite with a lighter, Th-enriched rim and a darker Th-depleted core (Type (2) ore). g) Elongated, slightly kinked monazite intergrown with hematite laths in Type (3) ore. h) Monazite and xenotime rim grains associated with a small apatite grain (Type (3) ore). i) Monazite porphyroblast (Type (3) ore) showing complex zonation with a Th depleted core (0.2 – 0.7 wt% ThO_2), an intermediate zone crowded with BSE bright spots, and a high Th rim (>5 wt% ThO_2). j) Strongly irregular, patchy zoned monazite with porous, sponge-like texture. Darker areas are enriched in S, Sr, and excess Ca, and are depleted in Th, P, and REE (Type (3) ore). k) Relict monazite from Type (4) ore partly replaced by a REE-alumino-phosphate (possibly florencite (Flo)) along the rim and cracks in the grain (Table 3). l) Patchy xenotime on an apatite grain rim from skeletal Type (4) ore. Mineral abbreviations are given in the Fig. 3 caption.

% (Table 4; Appendix 3). The monazite contains minor admixtures of SO_3 (b.d.l. – 0.25 wt%; Fig. 7b), SrO (b.d.l. – 0.25 wt%), and BaO (b.d.l. – 0.30 wt%). The PbO content in all analysed monazite grains is very low and does not exceed 0.04 wt%. The Y_2O_3 content varies between 0.40 and 0.80 wt%. Temperature estimates from the empirical Y-in-monazite geothermometer of Gratz and Heinrich (1997) for monazite co-existing with xenotime indicates a temperature range between 150 and 350 °C (Fig. 7c; Appendix 3).

Xenotime (Y_2O_3: 44.00–38.00 wt%) shows some enrichment in Dy_2O_3 (up to 6.90 wt%) and has a variable Yb_2O_3 content (3.00–4.10 wt %; Table 4; Appendix 3). It has variable concentrations of ThO_2 (<0.10–0.38 wt%) and UO_2 (b.d.l. – 0.31 wt%), which correspond to a Th/U ratio of <0.01 to 1.50. The $LREE_2O_3$ and $HREE_2O_3$ content in the xenotime ranges from 2.20 to 1.10 wt% and 18 to 21.20 wt%, respectively.

Zircon is a rare accessory phase and occurs mostly in intergrowths
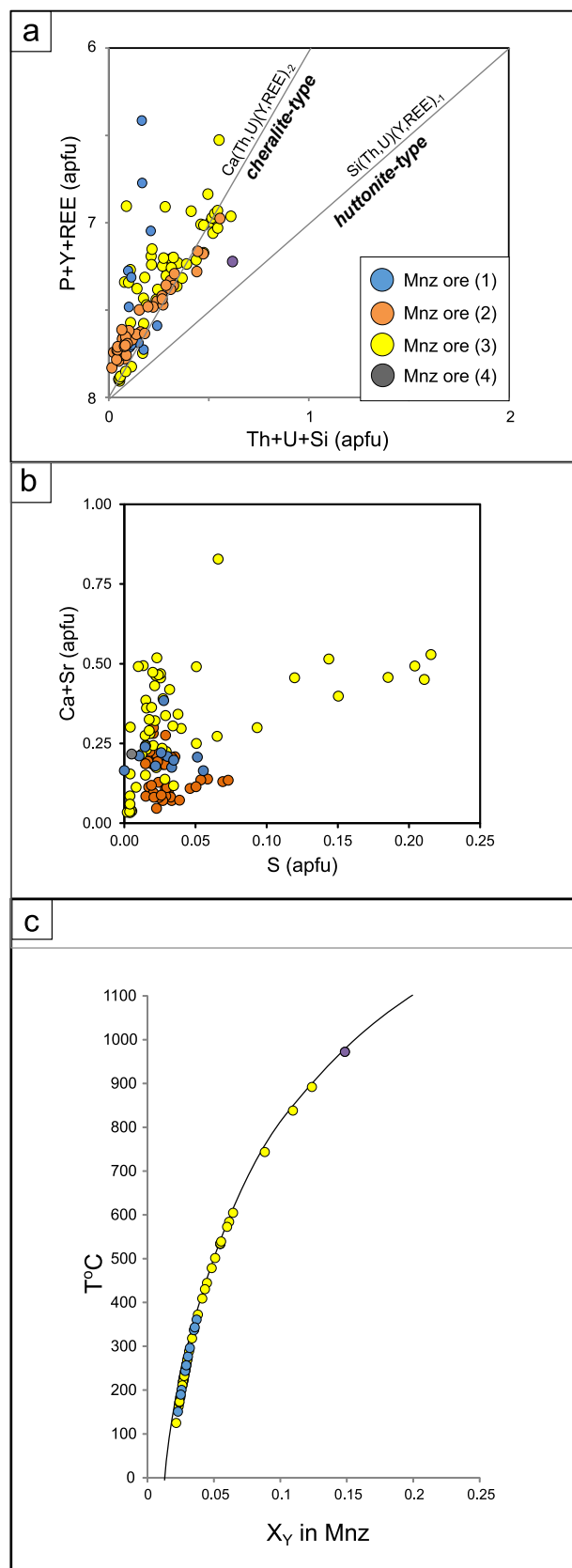
Fig. 7. Compositional variations in monazite from the PKF IOA ores. a) (P + Y + REE) vs. (Th + U + Si) (apfu) plot showing a predominant cheralite-type substitution as opposed to a huttonite substitution mechanism in the PKF IOA ore monazites. b) Relationship between the S and Ca + Sr content in the PKF monazites. Note the highly elevated content of S and Ca + Sr and their positive correlation in some monazites from the Type (3) ore. In contrast, enrichment in Ca and Sr in other ores is unrelated to S. c) X_Y in monazite versus temperature estimates plotted along the monazite limb of the monazite-xenotime miscibility gap after Gratz and Heinrich (1997) monazite-xenotime geothermometer. Note wide range of calculated temperatures in Type (3) ore monazite.

with magnetite or is enclosed in it. Zircon forms anhedral, angular, often fractured, unzoned grains ~10 to 20 μm in diameter.

Silicate minerals in Type (1) ore include white mica, biotite (partially replaced by chlorite), albite, and quartz in the matrix or as fissure infill. White mica was identified by WDS analysis as muscovite relatively high in Fe (up to 3 wt%) and low in Mg (Table 5). Biotite, as annite, is rich in Fe ($Mg^{2+}/(Mg^{2+}+Fe^{2+}) = 0.32$) and Cl (up to 2.5 wt%). Chlorite, as chamosite, contains high amounts of Fe (24–28 wt%).

4.2. Type (2) ore

Type (2) ore exhibits a foliated, banded structure, underlain by a flat-parallel arrangement of platy mineral grains. The segregation of grains into iron oxide and apatite- and silicate-dominated alternating thin layers is clearly marked (Fig. 3c, d). Type (2) ore is composed of approximately equal modal proportions of magnetite and hematite. Magnetite in the Fe oxide-dominated parts forms 50 to 100 μm diameter porphyroblasts with irregular lobate grain margins, whereas in the silicate domains it occurs as rounded crystals and aggregates 30 to 50 μm in diameter (Fig. 3d). Most of the magnetite grains are rich in silicate inclusions. Oriented specularite-type hematite is clustered into bands, which surround the magnetite porphyroblasts or form individual hematite-rich thin layers up to 1 mm thick.

In Type (2) ore, apatite occurs in discontinuous apatite-rich lenses and clustered accumulations of various sized grains (250–10 μm; Fig. 4c). Some apatite grains show a faint spotty zonation under BSE imaging (Table 3; Appendix 2). Fluorapatite predominates and, in comparison to Type (1) ore, is higher in OH and lower in Cl (Xo_{H-Ap} up to 0.30; Cl < 0.52 wt%; $X_{Cl-Ap} < 0.1$; Fig. 5a). The SrO, BaO, and MnO concentrations do not exceed 0.25, 0.22, and 0.15 wt%, respectively (Table 3; Appendix 2) whereas the total Y + REE content is <0.2 wt% (Fig. 5e).

The only accessory REE phase in the Type (2) ore is monazite. It occurs mostly as relatively large (50–80 μm) ameboidal grains with lobate grain boundaries, often elongated parallel to the lineation of the surrounding phyllosilicates and hematite (Fig. 6e). Monazite grains occur in groups usually in the vicinity of the magnetite-hematite and thin apatite layers (Fig. 6e), but also as intergrowths with apatite (Fig. 6f). The monazite is low in ThO_2 (0.10–2.00 wt%; Table 4; Appendix 3), but lighter rims or patches in some grains (Fig. 6f) contain higher amounts of ThO_2 (2–6.10 wt%). Similar to monazite from Type (1) ore, the predominant Th substitution mechanism is the cheralite substitution (Fig. 7a). The UO_2 concentrations are consistently very low (<0.1 wt%) and the Y_2O_3 content varies between 0.4 and 0.8 wt% (Appendix 3). Moreover, monazite from the Type (2) ore exhibits a variable SO_3 (up to 0.30 wt%;) and BaO content (sporadically up to 0.67 wt%). The PbO content does not exceed 0.1 wt% and in most cases is near or even below the EPMA detection limit.

Silicate phases are represented by white mica, chlorite, quartz, and locally plagioclase. Plagioclase is compositionally close to albite and contains minor amounts of FeO (up to 0.50 wt%) and SrO (0.02–0.15 wt%; Table 5). In comparison with Types (1) and (3) ore, the muscovite show enrichment in Fe and Mg and an evolution towards phengite (FeO: 3.50–5.60 wt% and MgO: 1.10 wt%; Table 5). Quartz occurs as polycrystalline thin layers and lenses, sometimes as elongated

(caption on next column)

porphyroblasts.

4.3. Type (3) ore

Type (3) ore has an augen gneiss appearance and seems to be an intermediate member between the brecciated and banded ores (Fig. 3e). Texturally, the banding is characterised by the elongation and orientation of the mineral grains. Segregation between the iron oxide, apatite, and silicate domains is visible on the scale of the thin section, albeit less pronounced than in the Type (2) ore. Augens in the gneiss consist of porphyroblasts of magnetite (50–300 μm), which are surrounded by platy to fibrous minerals (Fig. 3f). The magnetite porphyroblasts contain swarms of silicate and apatite inclusions, especially in the outermost zone of the magnetite porphyroblast. Specular hematite forms lath-like, elongated crystals, which wrap around the magnetite porphyroblasts and the surrounding fibrous minerals.

The distribution of apatite in the Type (3) ore is more random than in the Type (2) ore and occurs as anhedral grains 200 to 50 μm in diameter in a hematite-silicate matrix (Fig. 4d) or within crosscutting quartz veins. Some apatite grains are homogenous, whereas others show a textural heterogeneity in the form of lighter and darker patchy areas, spots, or veinlets (Fig. 4f). Distribution of these domains occurs mostly along the margins, whereas in some cases lighter zones are found in the central parts of the apatite grains, especially in the vicinity of fissures in the grain. The boundary between the darker and lighter zones is gradual and blurred. The apatite has a more diversified composition compared to apatite from Types (1) and (2) ore (Table 4; Appendix 2). This includes higher Cl concentrations (up to 3.10 wt% and X_{Cl-Ap} up to 0.45), lower F concentrations, and a higher admixture of OH (on average $X_{OH-Ap} = 0.25$; Fig. 5a). Concentrations of MnO and SrO vary between 0.25 and 1.05 wt% and 0.15 to 1.20 wt%, respectively, and both oxides are positively correlated with each other (Fig. 5b). MnO shows a weaker increase with increasing Cl content in the apatite then SrO (Fig. 5c and d, respectively). In texturally heterogenous grains, the lighter zones show enrichment in Sr, Mn, and Cl compared to the darker zones. The Y + REE content does not exceed 0.40 wt% $(Y + REE)_2O_3$ (Fig. 5e).

Monazite in Type (3) ore occurs in various textural contexts. These include inclusions in, and intergrowths with, magnetite or hematite (Fig. 6g) and as overgrowths or rim grains on apatite (Fig. 6h). Monazite intergrown with hematite show the same orientation and elongation as the hematite, and usually does not exceed 50 μm in diameter (Fig. 6g) except for rare, up to 100 μm size grains (Fig. 6i). Smaller monazite grains are generally texturally homogenous, similar to that seen in Type (2) ore, though a subset are characterised by BSE dark cores and light rims (Fig. 6i). The border between these zones is irregular, often cuspate. Additionally, some monazites have a patchy, irregular zonation (Fig. 6j). Monazite in Type (3) ore generally has a high ThO_2 content (2.00–6.50 wt% ThO_2; Table 4; Appendix 3), though the inner domains in some grains contain <1.00 % ThO_2. The cheralite-type substitution predominates (Fig. 7a). In some grains excess Ca-enrichment, as well as SrO (up to 0.5 wt% and 0.08 apfu), are correlated with the elevated S content (up to 1.00 wt% and 0.22 apfu; Fig. 7b). The Y_2O_3 concentration per monazite grain can vary from 0.40 wt% up to 2.6 wt%, which results in a wide range of temperatures (125–800 °C) utilising the monazite-xenotime geothermometer of Gratz and Heinrich (1997) (Fig. 7c; Appendix 3). The majority of the monazite grains have a low Pb content (b. d.l. – 0.03 wt%), except for a few grains containing between 0.2 and 0.6 wt%, which is uncorrelated with the Th and U concentrations. This made dating of these monazite grains untenable. In the zoned monazite grains (Fig. 6i), the rims are enriched in Th and Ca and depleted in REE with respect to BSE darker cores, whereas the behaviour of Y and Pb show no obvious trend. Additionally, the patchy zonation is reflected by differences in the Ca, S, and Sr content (Fig. 6j). Some zoned grains are intergrown with BSE bright, very small, Th-rich inclusions (<2 μm), which most likely are monoclinic huttonite ($ThSiO_4$) (Harlov et al., 2007).

Xenotime is less common than monazite and occurs both as small inclusions (<10 μm) in magnetite, and as anhedral, often porous, or even skeletal grains on the rims of the magnetite and hematite grains, and rarely on apatite grain rims (Fig. 6h). Xenotime shows a variable ThO_2 (b.d.l – 0.25 wt%) and UO_2 content (<0.10–0.30 wt%), and subsequently a wide range in the U/Th ratio (<0.01–1.60; Table 4, Appendix 3).

Silicate minerals are represented by chlorite, muscovite, quartz, and albite. Chlorite and white mica occur as strongly elongated platy or fibrous aggregates. The composition of the white mica (muscovite) and the chlorite (chamosite) is almost identical to that found in the Type (1) ore. Quartz and albite occur as fine, recrystallised aggregates and thin layers between the iron oxides as well as porphyroblasts. Rare accessory zircon forms faint zoned angular or rounded crystals ranging in diameter from 10 to 80 μm.

4.4. Type (4) ore

In the Type (4) ore, iron oxides show the lowest modal content compared to the brecciated, augen, and banded ore types. Iron oxides form dendritic veinlets within massive quartz (Fig. 3g). Magnetite is a relic phase, occurring as subhedral, randomly distributed grains overgrown and partly replaced by hematite. Maghemite takes the form of kinked, skeletal, elongated laths or blade-shaped crystals (up to 1.5 mm length) within coarse-crystalline quartz.

Apatite in Type (4) ore forms large, anhedral grains (up to 5 mm in size) with ragged boundaries, intergrown with hematite and quartz (Fig. 3h), locally disrupted. Compositionally, the apatite is similar to apatite in Type (3) ore (Table 3; Appendix 1). It displays high Cl concentrations (1.70–2.60 wt%; $X_{Cl-Ap} = 0.28–0.34$), low F (1.25–1.80 wt%; $X_{F-Ap} = 0.34–0.50$), and variable X_{OH-Ap} (0.18–0.34) (Fig. 5a). The apatite is enriched in SrO (0.60–1.10 wt%), MnO (0.85–1.10 wt%), and FeO (up to 2.20 wt%). It is possible that the high Fe content could be related to nano-inclusions of Fe-oxides. Manganese and Sr are positively correlated with each other (Fig. 5b) and Cl (Fig. 5c,d). The $(Y + REE)_2O_3$ content (0.10–0.23 wt%) does not differ from apatites in Types (1), (2), and (3) ore (Fig. 5e).

Monazite in Type (4) ore is scarce and occurs as fragmented grains within the iron oxides. It is replaced along fractures and grain boundaries by secondary REE-aluminophosphates with a composition close to florencite-Ce (Fig. 6k). Monazite has ThO_2 and UO_2 contents of up to 5.50 and 0.32 wt%, respectively (Table 4; Appendix 3), a relatively high huttonite component (Fig. 7a), and high Y_2O_3 concentrations (3.2 wt%) corresponding to an estimated temperature exceeding 900 °C (Fig. 7c; Appendix 3).

Xenotime is more abundant and occurs as aggregates (50–150 μm diameter) along apatite grain boundaries (Fig. 6l) or is dispersed as inclusions within the apatite. The UO_2 content ranges from 0.40 to 1.10 wt%, whereas ThO_2 is below 0.10 wt%, which is reflected in the low Th/U < 0.06. The xenotime has significantly elevated CaO (2.0–29.0 wt%) and F (0.1–0.50 wt%) contents (Table 4; Appendix 3).

5. Discussion

5.1. Evidence of a protracted metasomatic overprint recorded by apatite textures and mineral chemistry

Apatite in all four ore types is mostly anhedral with irregular, embayed grain boundaries. In some cases the apatite manifests a microporosity (Fig. 4e) and patchy, irregular structure (Fig. 4e, f) which are indicative of dissolution-reprecipitation processes (Putnis, 2002, 2009). Such a process, triggered by mineral-fluid interaction, is considered to be the main factor in the liberation of REE + Y from the apatite (Harlov and Förster, 2003; Harlov et al., 2005; Broom-Fendley et al., 2016). In IOA-type ores, the primary apatite displays an elevated REE content. However, in the altered zones of the ore system the REE concentrations

in the apatite decreases sharply as a result of a fluid-mediated leaching out of these areas during a coupled dissolution-reprecipitation process (Harlov et al., 2002; Bonyadi et al., 2011). A similar low REE content in apatite from all ore textural types (Fig. 5e; Table 3; Appendix 1) suggests that fluid-aided REE leaching occurred for the entire ore system (Jonsson et al., 2016). The rare presence of monazite and xenotime inclusions in PKF apatite, along with associated rim grains (Fig. 6c, h, l), is also due to a fluid-aided, coupled dissolution-reprecipitation process, which scavenges Th, U, REE, and P from the host apatite to form the monazite inclusions and rim grains. This spatial association of secondary accessory REE phases with apatite is a feature typical of fluid-mineral interaction in IOA deposits, such as at Kirunavaara (Harlov et al., 2002) or Grängesberg (Jonsson et al., 2016). Apatite metasomatism experiments have shown that NaCl- and CaCl₂-bearing solutions inhibit monazite nucleation within, or associated with, apatite (Harlov and Förster, 2003). This suggests that the leaching of REE away from metasomatised apatite was most likely facilitated by NaCl-bearing and CaCl₂-bearing fluids (Harlov and Förster, 2003; Harlov et al., 2005).

Assuming that apatite from the Type (1) ore has a composition closest to that of pristine apatite in these ore bodies, since it exhibits the lowest grade of alteration, deformation, and has a composition typical for unaltered or mildly altered IOA ores, the Cl-, Sr-, and Mn-rich apatite from Types (3) and (4) ore (Fig. 5b-f; Table 3) would suggest that in these two ore bodies the apatite has been metasomatically altered. A number of studies have shown that the partitioning of Cl between apatite and a fluid depends on the composition, salinity, and pH of the participating fluids, the apatite mineral chemistry, and the P-T conditions (e.g., Webster et al., 2009; Doherty et al., 2014; Kusebauch et al., 2015). For example, partitioning of Cl between apatite and a melt/fluid can increase with decreasing pressure (Zhu and Sverjensky, 1991; Doherty et al., 2014). At 0.2 kbar, the $D_{Cl}^{ap/fluid}$ and $D_{Cl}^{ap/melt}$ are 30 times lower than at 0.05 kbar for the same temperatures (Doherty et al., 2014). This is in contradiction with the situation within the BSZ, where those ores hosting Cl-enriched apatite are situated in the high strain zone. In the apatite-silicate, melt-fluid system at 900 to 924 °C and 2 kbar, Cl incorporation into apatite is strongly related to the Cl⁻ activity in the fluid (Webster et al., 2009) and the OH activity (Kusebauch et al., 2015). This has been documented in some IOA deposits from the Chilean iron belt during alteration of fluorapatite to Cl-OH or F-Cl-OH apatite due to Cl-rich fluids (Palma et al., 2019). Lastly, in simpler systems fluorapatite has been experimentally converted to near endmember chlorapatite in 1 to 2 M CaCl₂-bearing solutions at 900 °C and 10 kbar, whereas in NaCl- and KCl-bearing solutions, X_{Cl-Ap} decreases in altered areas (Harlov and Förster, 2003).

Chlorine-enriched apatite from Types (3) and (4) ore stands out in terms of its elevated SrO and MnO content (Fig. 5b-f; Table 3; Appendix 2), which are positively correlated with each other (Fig. 5b) and negatively with CaO (Fig. 5f) implying that the enrichment in Cl was coupled with an increase in Mn and Sr. The simultaneous enrichment in Cl, Mn, and Sr can be explained by the ability of Cl-rich solutions to mobilise Mn and Sr ions due to complexing with Cl⁻ (Williams-Jones and Heinrich, 2005), which has been documented for both magmatic and hydrothermal systems. In a magmatic environment, the enrichment of Sr in apatite is coupled with a higher Ca activity (Sha and Chappell, 1999) based on the substitution of Sr for Ca (Rakovan and Hughes, 2000) but was recognised especially in late-stage or altered apatite in peralkaline suites and carbonatites as the result of residual, CO_3^{2-} and/or halogen and LILE-enriched melts and associated volatiles (e.g. Chakhmouradian et al., 2002; Zhang et al., 2011). In some Chilean IOA ores, metasomatically induced Cl-enrichment in apatite (up to 6.70 wt% Cl) is simultaneous with enrichment in SrO (up to 0.3 wt%) in comparison with pristine fluorapatite (SrO < 0.06 wt%) (Palma et al., 2019; La Cruz et al., 2019). Unusually Mn-rich (30–51 wt% MnO) chlorapatite (i.e. pieczkaite) has been found in pegmatites from Szklary, Sudetes, Poland (Pieczka, 2007; Szuszkiewicz et al., 2018) and Cross Lake, Manitoba, Canada (Tait et al., 2015), which crystallised from extremely fractionated, Mn- and Cl-

enriched melts. Enrichment of Sr in apatite altered by carbonic, acidic, low-salinity hydrothermal fluids is associated with the development of orogenic gold deposits and is regarded as fingerprint of the ore-forming processes (Zhang et al., 2020). This is supported by the fact that the increase of Sr in altered areas of the apatite is coupled with the leaching of REE and Si, thereby implying the fluid-assisted mobilisation of the Sr. Thus, the enrichment of Cl, Mn, and Sr in apatite in Type (3) and (4) ores implies the interaction of the apatite with specific, locally occurring fluids that are saturated in those elements predominant in these ores.

5.2. Monazite and xenotime micro-textures as indicators of syn-tectonic mineral-fluid interaction

Monazites from the different ore types show pronounced differences in composition, (especially in terms of the Th and Y content) either as individual grains within a single body or even on the grain-scale (Appendix 2). In Type (1) ore, the monazites show the least compositional variability, whereas in Type (3) ore the highest variability is observed (Appendix 2). Monazite in Type (3) ore contains a higher average ThO₂ concentration compared to monazite from Types (1) and (2) ore (Appendix 2). In general, monazite formed under hydrothermal conditions will not contain a ThO₂ content>1 wt% (Schandl and Gorton, 2004). However, this is not a universal discriminating feature between high- and low-temperature monazite (Catlos, 2013). In apatite metasomatism experiments, monazite inclusions with an extremely high Th content reflect the high Th content in the host fluorapatite (Harlov and Förster, 2003). However, there is no evidence that apatite from the PKF ores was originally Th-rich. The secondary nature of Th-enrichment is evidenced by the textural and compositional heterogeneity displayed by some monazites, the presence of porosity, and irregular grain shapes (Fig. 6d, f, j, l), which are indicative of alteration during fluid-mineral interaction (e.g., Putnis, 2002, 2009; Harlov et al., 2011; Williams et al., 2011; Richard et al., 2015). Zones enriched in Th can occur as irregular patches within or rims around the monazite (Fig. 6f, i). In some monazite grains, the degree of alternation, Th-enrichment, or Th-depletion is complete, as evidenced by their homogenous compositions (Fig. 6e). Poitrasson et al (1996) reported a two- or three-fold increase in the Th content of monazite in granitoids affected by chloritisation and alkali-fluid alternation. Indeed, in Type (3) ore the biotite has been totally replaced by chlorite, though an analogous situation also occurs in Type (2) ore where Th-rich monazites are less common. This suggests that chloritisation may not be a decisive factor in Th enrichment. Experimental metasomatism of monazite by solutions with a wide compositional range indicates that in Cl-bearing solutions Th has a low solubility compared to the REE, whereas in alkali-bearing environments both Th and REE are highly soluble (Oelkers and Poitrasson, 2002; Schmidt et al., 2007; Harlov et al., 2011; Tropper et al., 2011, 2013; Mair et al., 2017). Enrichment in the huttonite component and subsequent depletion in REE, Ca, and Pb occurs for monazite metasomatised by alkali-bearing solutions (Harlov and Hetherington, 2010; Hetherington et al., 2010; Harlov et al., 2011). In the PKF, the Th content in monazite for all four ore types takes the form of the cheralite-type substitution (see Fig. 7a) (Förster, 1998), which suggests a high Ca activity in the intra-crystalline fluid and a comparatively lower Si activity. Formation of huttonite inclusions in metasomatised areas of some monazites dominated by the cheralite substitution suggests the highly localised mobilisation of Si (Hetherington and Harlov, 2008). Experimentally, incorporation of Th into monazite via the cheralite substitution has been accomplished by using CaCl₂ + SrCl₂ bearing solutions under high-temperature conditions (Seydoux-Guillaume et al., 2002). Therefore, the accumulation of Th during metasomatic alteration of the monazite most likely resulted from the very low solubility of Th-Cl complexes in the metasomatising fluids compared to REE-Cl complexes (Nisbet et al., 2018). The presence of Ca²⁺ and Cl⁻ as the main agents behind monazite alteration agrees with observations made regarding the metasomatic alteration of apatite from Types (3) and (4) ore.

In some monazites, especially those from Type (3) ore, the altered domains show a high Ca, S, and Sr content (Fig. 6j and 7b; Appendix 3). Calcium and S are incorporated into the monazite structure in the form of clinoanhydrite ($CaSO_4$) via the coupled substitution: $Ca^{2+} + S^{6+} = (Y + REE)^{3+} + P^{5+}$ (Crichton et al., 2005; Laurent et al., 2016). This substitution mechanism seems to be also responsible for the subsequent enrichment in Sr (Chen et al., 2017). Secondary monazite with a high S and Sr content has been reported in some carbonatite systems by Broom-Fendley et al. (2020; up to 11.5 wt% SO_3 and 5.7 wt% SrO) and Chen et al. (2017; >4 wt% SO_3). In a metamorphic magnetite deposit at Bacuch, Western Carpathians, Slovakia the monazite-(Ce) is very rich in SO_3 (>11 wt%) and SrO (>8 wt%), and is proposed to have originated from a hydrothermal overprint related to sulfide ore mineralisation (Pršek et al., 2010). A reaction between primary monazite and oxidising As- and S-bearing fluids in rare metal-bearing rhyolites from Tisovec-Rajkovo, Western Carpathians, Slovakia caused the formation of an arsenian monazite-phosphatian gasparite ($LREE(As,P)O_4$) solid solution, containing up to 0.95 apfu As and up to 0.14 apfu S (Ondrejka et al., 2007). Sulfur enrichment in monazites from Type (3) ore could have been due to the presence of sulphate ions resulting from the oxidation of accessory pyrite or chalcopyrite.

The elongated orientation of the monazite parallel to the rock foliation in Types (2) and (3) ore suggests that deformation could have played an important role in the modification of the monazite morphology and mineral chemistry. Changes in the monazite mineral chemistry in deformed rocks can also be promoted by a dissolution-reprecipitation creep phenomenon (Wawrzenitz et al., 2012), which results from the coupling of fluid-aided dissolution-reprecipitation with strain. Rocks from the PKF show varying degrees of deformation, which suggest that the degree of monazite alteration was affected by the strain rate (Wawrzenitz et al., 2012). Indeed, high Th monazite (up to 6.4 wt% ThO_2) is found in Types (3) and (4) ore, which are located in the lower structural levels of the BSZ. These levels experienced a higher degree of deformation than Types (1) and (2) ore in the upper structural levels, which were dominated by brittle, lower temperature deformation.

While monazite rarely co-exists directly with xenotime in the PKF ore bodies, the similar textural position of these two phases, within the matrix or as inclusions in magnetite, suggest a cogenetic origin. Monazites from xenotime-bearing samples contain a relatively low but variable Y and HREE content (Table 4; Appendix 2). For the apparently least altered monazites from Type (1) ore, monazite-xenotime temperature estimates cluster around 250 to 350 °C, whereas in the Type (3) ore they are scattered between 120 and 890 °C (Fig. 7c). In the Type (4) ore one monazite gave a temperature >970 °C (Fig. 7c). The wide range in monazite-xenotime temperatures in the Type (3) ore suggest a certain amount of disequilibrium between the monazite-xenotime pairs due to Y + REE mobilisation, though this broad temperature range does include the temperatures associated with the plastic deformation of quartz in the BSZ metasediments, which ranged from 350 to 450 °C, and up to 500 °C in the highest strain rocks during regional shearing (Schneider et al., 2019). Variable enrichment or depletion of Y in monazite during alteration explains the unrealistically high temperatures of >800 °C, (granulite facies metamorphism), estimated for some Y-rich monazite grains, as well as temperatures as low as 120 °C for Y-poor monazite. Although there is no cross correlation between the textural position of monazite in a given ore type (i.e. silicate-oxide matrix vs. inclusion in another mineral), the range of obtained temperatures in the least tectonically reworked Type (1) ore is much narrower than in Types (2) and (3) ore, highlighting the unclear relationship between the degree of deformation vs. metasomatic alteration. Nevertheless, the temperatures estimated for Type (1) ore are comparable with those constrained by secondary monazite in the Pea Ridge deposit (50 to 400 °C; Harlov et al., 2016), or in the Bafq District (300 to 400 °C; Taghipour et al., 2015), and are also supported by fluid-inclusion studies of the BSZ formation (Schneider et al., 2019), which formed in the same approximate temperature range.

The relatively monotonous composition of xenotime in Types (1) and (3) ore suggest that the response of xenotime to the solutions infiltrating these IOA ore bodies was much less extensive than that experienced by monazite under the same P-T-X conditions. However, certain variations in the composition of individual xenotime grains, especially with respect to the U and Th concentration (Table 4; Appendix 3), as well as the heterogenous texture of the grains (Fig. 6d), indicate that some limited alteration did occur. Variabilities in the xenotime Th/U ratio <0.01–1.62 could have resulted from subtle local differences in the fluid chemistry, and subsequently differences in Th and U mobilisation (McNaughton and Rasmussen, 2017). This has been demonstrated in xenotime metasomatism experiments involving a wide range of fluids (brines, alkaline, and acidic) in conditions corresponding from medium to high grade metamorphism (Hetherington et al., 2010). However, in experiments involving alkali-bearing fluids under high pH conditions supersaturated with Th, Th has been remobilised and incorporated into xenotime (Harlov and Wirth, 2012). Only xenotime in Type (4) ore stands out in terms of a high U-content, reaching 1.1 wt% UO_2. These same xenotime grains also show a low Th content and a striking depletion in LREE compared to xenotime from Types (1) and (3) ore (Table 4; Appendix 3). The UO_2 enrichment in xenotime can be explained as the result of the metasomatic addition of U to xenotime under oxidising conditions (Xing et al., 2018), which is supported by the predominance of hematite in Type (4) ore. Grainy xenotime aggregates (Fig. 6l) locally show a very high Ca content (up to 29.0 wt%; Appendix 3) and enrichment in F (up to 0.51 wt%), suggesting the presence of minor amounts of Y-HREE-bearing apatite micro- or nano-inclusions. These could represent remnants of the parental apatite or products of partial metasomatic alteration of xenotime in the presence of localised Ca-rich fluids (Budzyń et al., 2017; Budzyń and Sláma, 2019), which supports the scenario that these four ore types were infiltrated by Ca-bearing fluids. Absence of other typical products of xenotime breakdown, such as Y-HREE-britholite or Y-HREE-epidote, may be due to the very low modal amount of aluminosilicates in the ore bodies (Budzyń et al., 2017; Budzyń and Sláma, 2019).

5.3. The PKF ore bodies as IOA-type deposits

The ore bodies occurring within the BSZ show features characteristic of IOA deposits: (1) they are composed primarily of magnetite (+/- hematite) and lesser apatite; (2) they are spatially related to igneous rocks, in this case metagabbros; (3) they contain trace amounts of Cu-sulphides (Williams, 2010); and (4) the trace element content in the magnetite is low, especially with respect to Ti, Cr, (each <0.5 wt%) and Ni (<0.1 wt%) (Dare et al., 2014; Dupuis and Beaudoin, 2011). These criteria help to discriminate these particular IOA ore bodies from other igneous Fe- and P-bearing ore types, such as Fe-Ti-P ± V ores or nelsonites, which are characterised by a high-Ti oxide assemblage made up of Ti-bearing (>10 wt%) magnetite ± ilmenite (e.g. Charlier et al., 2015) along with REE-rich (up to 3 wt% REE) fluorapatite (Dymek and Owens, 2001). Nelsonites are normally associated with ultramafic rocks, especially anorthosite or gabbronorite suites. Their genesis is principally linked with purely magmatic processes (see Charlier et al., 2015 for the review). These can include immiscibility between an ultramafic and a Fe, Ti, and P-rich magma (Philpotts, 1967; Kolker, 1982); fractional crystallisation, segregation, and phenocryst accumulation (e.g. Duchesne, 1999); or the interplay of both processes (Namur et al., 2012) without the significant involvement of a fluid phase and subsequent metasomatic overprint. All genetic models describing IOA-type mineralisation consider the importance of high-temperature fluids in the transport and deposition of Fe, P, Ca, and REE as well as the subsequent interaction of the crystallised magnetite and apatite with these and later fluids (Corriveau et al., 2016; Harlov et al., 2002, 2016; Huang et al., 2019; Hu et al., 2019). However, the composition of these fluids, the extent of alteration, and the resulting secondary mineral assemblages is unique to each individual deposit.

Low-Ti, low-V magnetite and apatite assemblages, including REE

phosphates, can also occur in other types of ore deposits, which are genetically distinct from IOA ore deposits. These include carbonatites and iron skarns (Zhou et al., 2022; Hawkins et al., 2016); metamorphogenic-hydrothermal mineralisation, such as the Bacuch magnetite deposit in the Western Carpathians (Pršek et al., 2010); or metamorphosed banded iron formations (BIFs) (Nutman and Friend, 2006). Although skarns are genetically connected with igneous intrusions into carbonate-rich sedimentary rocks, they are characterised by more or less polymetallic mineralisation, and the Fe is associated with a variety of other metals, such as Zn, Pb, Mo, or W. This is in obvious contradiction with the sulphide-poor, almost pure Fe character of the PKF IOA ore bodies. Moreover, the lack of a contact metamorphic aureole between the metagabbros and the metasedimentary host, and the absence of gangue minerals typical for skarns, such as wollastonite, diopside, grossular-andradite garnet, among others, exclude a skarn affiliation for the PKF IOA ores. In the case of the Bacuch magnetite deposit, the mineral assemblage is much more diversified. Here the monazite and xenotime formed coevally with the magnetite and the sulphides, independent of the apatite (Pršek et al., 2010). BIFs are characterised by their larger, regional extent, and despite metamorphic reworking, the original banded Fe-oxide-quartz sedimentary structures are preserved (e.g. Bekker et al., 2010). In contrast, the banding observed in types (2) or (3) ores results solely from deformation and metamorphic segregation of select mineral phases. To conclude, among all of these alternative scenarios, the identification of the PKF ore bodies as IOA ore bodies of the Kiruna-type would appear to be the best match to the data.

5.4. Mafic magmatism and ore mineralisation in Prins Karls Forland

The genetic association of IOA deposits with volcanic or subvolcanic magmatic suites would suggest that they originate when iron oxide-phosphate-dominated and silicate-dominated magmas become separated from each other during magmatic differentiation, most likely due to immiscibility. An extremely elevated Fe content in the parental magma is one of decisive factors controlling unmixing in a silicate liquid (e.g., Naslund, 1983). The miscibility gap can be further enlarged by the presence of P, Ti, and alkalis (Visser and Koster van Groos, 1979;
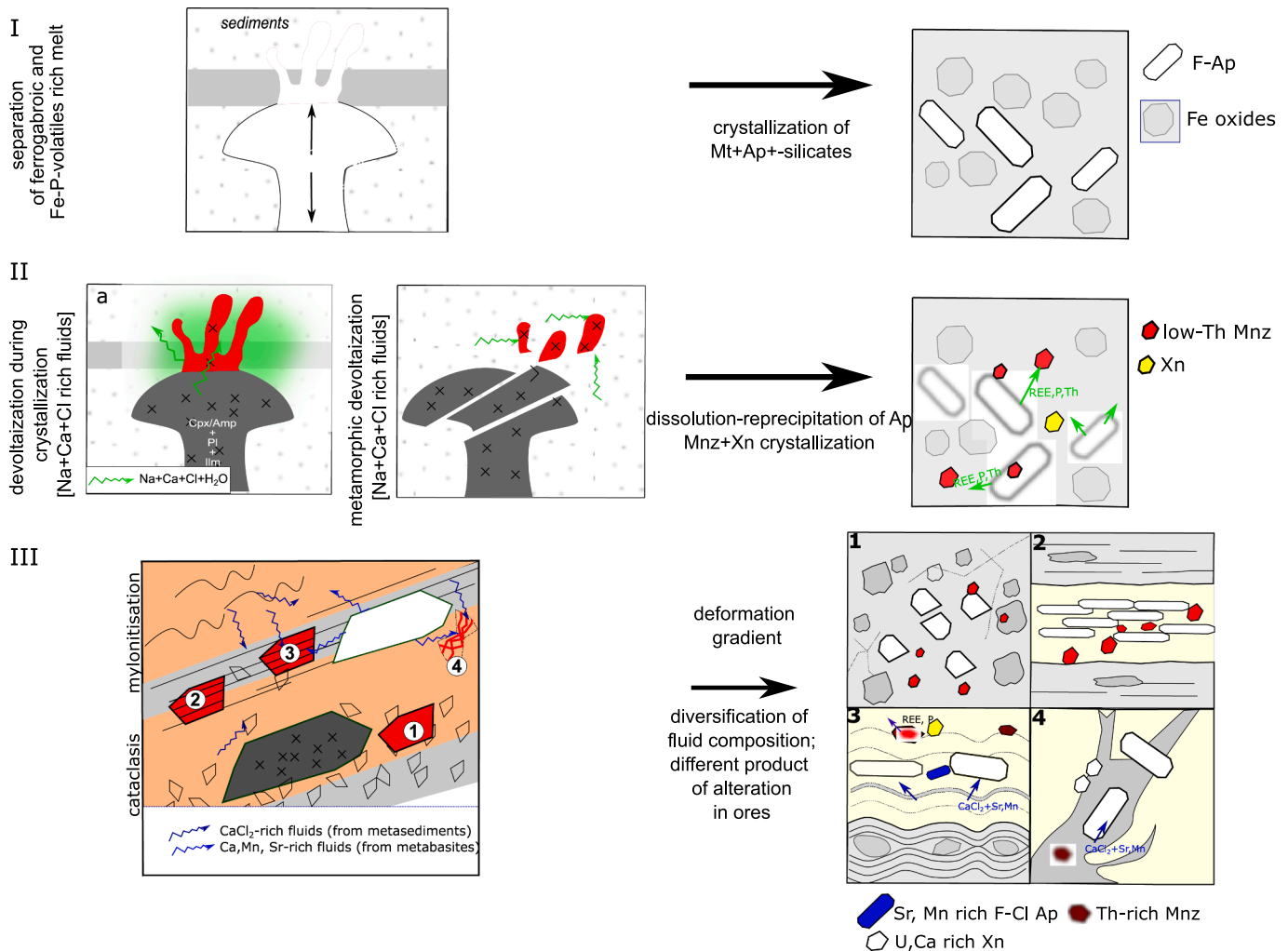
Fig. 8. Scheme illustrating the proposed model of formation and reworking of IOA-type ore bodies in the PKF. Stage I – separation of Fe-P-REE fluid-rich residual magma from the gabbroic melt due to immiscibility between the mafic silicate magma and a Fe-P-Ca-REE-rich hypersaline fluid, resulting in the emplacement of Fe-oxides (magnetite) and REE-rich fluorapatite. Stage-II – First stage of alteration of the IOA ores resulting in the metasomatic alteration of the primary Y + REE rich fluoarapatite and the crystallization of monazite and xenotime connected with a) late-magmatic expulsion of fluids from the cooling magmatic body or b) regional metamorphism of the hosting metasedimentary units. Stage-III – Second stage of alteration involving the metasomatic enrichment of fluorapatite with Mn, Sr, and Cl and the enrichment of monazite in Th (and locally S) from those ores emplaced in the higher grade levels of the BSZ. At the same time there is a lack of significant mineral modifications in those ores situated relatively remote from the metagabroic bodies. In the higher grade levels, the more extensive reworking of metamafites and/or hosting metasediments triggered expulsion of CaCl₂-bearing, and Sr-Mn-S-enriched fluids allowing for the modification of the minerals. The strain gradient across the BSZ resulted in the modification the ore textures. Numbers 1 – 4 represents Types (1) – Type (4) ore bodies.

Charlier and Grove, 2012) as well as a high H_2O (10 wt%) and F (0.2–6 wt%) content (Lester et al., 2013; Hou et al., 2018). This phenomenon of immiscibility, supported by fractional crystallisation and crystal accumulation, is thought to be the main process behind the Fe-Ti-P mineralisation associated with mafic (ferro)gabbroic cumulates from the Sept Iles layered intrusion in Canada (e.g., Namur et al., 2012), from the Skaergaard layered intrusion in Greenland (McBirney and Nakamura, 1973), or with the Vergenoeg Pipe, Bushveld Complex, South Africa (Hou et al., 2017).

Although layered mafic intrusions are large-scale magmatic suites, the metagabbros in the BSZ shear zone, associated with the IOA ore bodies, are relatively small, and most likely originated as dykes. They show many features similar to ferrogabbroic cumulates in layered mafic intrusions. These include Fe oxides with a high Ti content (ilmenite) associated with apatite as an intercumulus phase, due perhaps to immiscibility of the parental magma. The enigmatic provenance of the metasedimentary rocks in the PKF hosting both the metagabbros and the IOA ore bodies, coupled with their occurrence in a tectonic melange, suggest that they could be part of a more extensive complex that was uprooted during thrusting.

In the least altered/deformed metagabbro bodies of the BSZ shear zone, pargasite occurs as an intercumulus phase indicating that crystallisation or decompressional re-equilibration of the original gabbro took place at a relatively shallow crustal level involving a water-rich melt (Klaver et al., 2017), which could be a solvable environment for the separation of silicate and ferrous magmas. In turn, enrichment of H_2O and halogens in the magma would facilitate the complexation and mobility of Fe, as well as REE and P (Knipping et al., 2015), enhancing the immiscibility of a Fe-Ca-P-rich fluid/melt from the silicate magma and its emplacement in the surrounding metasediments (Hou et al., 2018; Stage I in Fig. 8). Moreover, the metagabbros are rich in ilmenite, whose early crystallisation and fractionation could have contributed to the fractionation of the Ti-poor, Fe-P melts responsible for the IOA mineralisation at low pressure and temperatures and high fO_2. In contrast, the effective separation of Ti-rich, Fe-P magmas corresponding to a nelsonite requires a high pressure, temperature, and lower fO_2 (Lledo et al., 2020). The overall low Ti content in the magnetite from the metagabbro reflects the partitioning of Ti into ilmenite in the cumulate, though it could also represent formation of magnetite at low temperatures associated with a fluid phase (Nadoll et al., 2014). Lastly, a low Ti content in the magnetite could also indicate the recrystallization of the magnetite in a halogen-rich metamorphic fluid at low temperatures such that the Ti remained in the fluid by complexing with both the F and Cl (Rapp et al., 2010).

5.5. Reconstruction of tectonothermal history and the nature of the associated metasomatism

Metasomatic liberation of REE from apatite in IOA deposits could occur during the release of fluids from the H_2O-saturated, Fe-P-rich melt/fluid (Hou et al., 2018; Tornos et al., 2016; Stage IIa in Fig. 8). These volatiles are often high-temperature, saline, and alkaline or alkali-calcic as documented in El Laco (Broman et al., 1999; Tornos et al., 2016), in the magnetite-apatite deposits along the Middle and Lower Yangtze River, China (Li et al., 2015), or in the Choghart ore deposit, Bafq District, Iran (Khoshnoodi et al., 2017). For example, the involvement of an evolving magmatic-hydrothermal fluid during metasomatism is evinced by the Sr-Nd isotopes in the apatite from the Chaz-Gaz deposit in the Bafq District (Sepidbar et al., 2022). Crystallization of the mafic magma could also lead to the additional release of a significant volume of volatiles, especially considering the presence of intercumulus pargasite in the metagabbro suggesting a high H_2O content in the melt.

Another possibility is that the metasomatic fluids were not directly connected with the formation of the ore bodies themselves but rather were released from the surrounding metasedimentary rocks during a regional, tectonothermal event such as the Ellesmerian amphibolite-facies metamorphic event (Stage IIb in Fig. 8). Prograde metamorphism of sedimentary rocks and coeval devolatilisation would release fluids with a wide range of salinities, depending on the nature of the sedimentary protolith (Yardley and Graham, 2002). In the case of the Pinkie unit metapelites, the reaction of muscovite, chlorite, and quartz to produce garnet and staurolite would have released H_2O. However, there is no clear mineralogical evidence in the metagabbros that they were affected by regional amphibolite-facies metamorphism coevally with the host metapelites and metamarbles. The observed assemblage of hastingsite-edenite, actinolite, epidote-clinozoisite, albite, biotite, and titanite, replacing primary magmatic pargasite and plagioclase, developed during greenschist facies metamorphism or hydrothermal alteration (see below). Hence, the first stage of metasomatic alteration in the PKF ore bodies could have occurred shortly after the emplacement of the gabbros due to the expulsion of magmatic-hydrothermal fluids during crystallization. However, the interaction of metamorphic fluids released by metasediments during amphibolite facies Ellesmerian metamorphism cannot be ruled out. The main obstacle in solving this problem is the unknown age of the gabbros and the ores. However, the metasedimentary package hosting the metagabbros has a Tonian maximum deposition age of ~950 Ma (Kośmińska et al., 2015), which provides an indirect line of evidence for a post ~950 Ma age of the emplacement. Late Devonian, Ellesmerian metamorphism provides the other bracket for timing the emplacement of the gabbro, which would then place it between the Tonian and the Devonian.

The final stage of evolution (Stage III in Fig. 8), which resulted in the metasomatic alteration of the apatite and monazite via NaCl-, $CaCl_2 \pm SrCl_2$-, Mn-, and S-bearing fluids, had a different impact on each of the four IOA ore bodies depending on their position within the shear zone. It points to a *syn*-tectonic fluid circulation that was likely coeval with the formation of the BSZ itself during Eurekan tectonism. Crustal-scale shear zones, such as the BSZ, are the preferred avenues for channelized fluid flow in the lower and middle crust. Such shear zones enable long-distance, open-system metasomatic processes (Carter and Dworkin, 1990; Ague, 2014). In contrast, during coeval regional metamorphism and tectonism, dehydration-related fluid flow is usually dispersed, which leads to fluid-rock interaction being restricted to grain boundaries, limited exchange of fluids, and predominantly closed-system volatile circulation (Ague, 2014). Thus, advanced crustal-scale deformation, as manifested by the BSZ, is a plausible mechanism, which would have allowed for extensive fluid exchange between the metasedimentary rock, the gabbros, and the ore bodies.

Structural and $^{40}Ar/^{39}Ar$ geochronological data point to the development of the BSZ between 55 and 44 Ma. The temperatures during this deformation, based on quartz microstructures, are estimated at 300 to 350 °C, but they could have reached >500 °C in the highest-strain, mylonitised samples (Schneider et al., 2019). Even in such low- to medium-grade conditions, minerals such as apatite (e.g. Henrichs et al., 2018) or monazite (e.g. Seydoux-Guillaume et al., 2012; Richard et al., 2015) can undergo significant modification in a fluid-rich environment. The alteration of monazite is documented in the Pinkie metasediments, where some of the grains have been replaced by REE-apatite-allanite coronas (Kośmińska et al., 2020).

The mineral assemblages, which could have served as sources of Na, Ca, and Cl, are found in both the metasediments and the metagabbros. In the metapelitic and carbonate-dominated sequences belonging to the Craigtoppane Formation, Manby (1983b) described Cl-rich (up to 2.6 wt %), scapolite porphyroblasts, discordant to the biotite-almandine mineral fabric, which crystallised from Na^+, Ca^{2+}, Cl^-, and CO_3^{2-} fluids released during the second stage of metamorphism. Cl-rich scapolite (marialite) forms in a high grade, high salinity environment via a reaction between anorthite, halite, and calcite (Almeida and Jenkins, 2017). The protoliths of the PKF metasediments were probably shallow-marine deposits, which generally are characterized by the presence of evaporates. The stability of Cl-rich scapolite is sensitive to subtle changes in the salinity of the fluid (Almeida and Jenkins, 2019). This

implies that changes in the composition of the fluids derived from the PKF metasediments during both prograde and retrograde amphibolite-facies metamorphism, as well as during the following Eurekan deformation event and associated low-grade overprint, could have affected the stability and composition of the Cl-rich scapolite, and resulted in the subsequent liberation of Cl similar to what has been seen in scapolite from high-pressure amphibolite facies, calc-silicate sequences in Sare Sang, Afghanistan (Faryad, 2002). Here the fluids connected with retrogression were characterised by being the most Cl-saturated due to instability and breakdown of marialite with decreasing pressure.

In the metagabbros, alteration by Cl-bearing fluids (Stage III in Fig. 8) is evinced by a secondary assemblage consisting of Cl-rich amphiboles, Cl-rich biotite, actinolite, albite, clinozoisite-epidote, titanite, and scapolite (Appendix 1). Amphiboles in the metagabbros show a textural and compositional variability. Apart from veinlets of poikilitic, intercumulus pargasite, overgrowths of blue-green ferrohastingsite-ferroedenite also occur. Poikilitic pargasite shows a weakly elevated Cl content (b.d.l. – 0.5 wt%), whereas the ferrohastingsite-ferroedenite is characterised by elevated Cl ranging from 1 to 3 wt%. The occurrence of preserved pargasite in the metagabbros as platy, uniform poikilocrysts supports an igneous origin. Single relicts of clinopyroxene suggest the growth of pargasite via destabilisation of pre-existing clinopyroxene by reaction with a volatile-rich residual magma during decompression (e.g. Klaver et al., 2017; Smith, 2014).

Chlorine-rich amphiboles from the ferro-magnesio-hastingsite-edenite group, as secondary phases, are especially abundant in the Laurantzonfjellet section metagabbro bodies (Maraszewska et al., 2016). This section experienced the most extensive deformation including local protomylonitisation and advanced Cl-aided alteration as characterised by the presence of other Cl-phases, such as Cl-rich scapolite (Appendix 1). Despite the fact that the primary mineral assemblage in the original gabbros included pargasite and chlorapatite, their breakdown during metamorphism probably would not be able to liberate sufficient quantities of Cl into the fluid to significantly modify its composition on a larger scale, since chlorapatite occurs only as accessory phase, and the pargasite has a low Cl content (<0.5 wt%; Appendix 1). The Ca^{2+} was either derived from the surrounding metacarbonates, or from the albitisation of the labradorite in the metagabbro (Appendix 1). Thus, the Cl must have had been derived from an external source, such as the surrounding metasedimentary complex (Stage III in Fig. 8). Secondary Cl-rich parageneses in the meta-igneous rocks represent the effect of this alteration, not the source.

Metasomatic alteration of the Laurantzonfjellet metagabbros during metamorphism and deformation seems to be the most probable source of the Sr and Mn later incorporated into the apatite from Types (3) and (4) ore. Here, the breakdown of primary pargasite and plagioclase could have caused the release of Sr, whereas replacement of ilmenite (containing up to 2.6 wt% MnO; Appendix 1) by titanite could have introduced Mn into the fluid. Both elements would have been transported as Cl complexes (Williams-Jones and Heinrich, 2005), or/and as complexes with CO_3^{2-} released during strain-induced dissolution of cataclysed metacarbonates. Utilizing these fluids, the Mn and Sr could have then infiltrated both Type (3) and (4) ore, situated only a few meters away from these deformed metagabbros, where they were incorporated into the apatite and monazite (Table 1; Fig. 1; Stage III in Fig. 8). This also could explain why Type (1) ore, associated with least altered and deformed igneous rocks, and Type (2) ore, situated relatively remote from the metagabbroic bodies, did not experience Sr-Mn metasomatism. Lastly, interaction of these fluids with accessory sulphides in the IOA ore bodies and/or in local metasediments could have led to a local elevation in SO_3^{2-} causing variable S enrichment in the monazite.

Overall, the volatiles released during metamorphism tend to be characterised by a high compositional variability, which is reflected in the compositions of the minerals resulting from them, even on the thin-section scale (Kullerud and Erambert, 1999; Kullerud et al., 2001; Faryad, 2002). Hence, considering that the geological history of the study area is still relatively unknown, the model elaborated on above and in Fig. 8 should be treated as the simplest explanation based on the geochemical, petrological, mineralogical, and field data currently on hand.

6. Implications and conclusions

IOA- or Kiruna-type ore deposits are a strongly diversified group of worldwide ore deposits with a controversial genetic model. Currently, a magmatic origin, coupled with concurrent and subsequent metasomatic processes, seem to be the most likely scenario describing their formation. The IOA ore bodies within the Boureéfjellet Shear Zone, Prins Karl Forland, Svalbard are genetically associated with amphibole-ilmenite gabbroic cumulates. We propose that these ore bodies originated from the fractionation of Fe, P, Ca, and REE into hypersaline fluids associated with a gabbroic magma per some version of the flotation model proposed by Knipping et al. (2015) (Fig. 8). The presence of secondary REE phases in the IOA ore bodies, such as monazite, xenotime, and allanite, were metasomatically derived from the original REE-bearing fluorapatite most likely as a result of devolatilisation of the magma during or shortly after their emplacement alternatively associated with fluids released during regional amphibolite facies metamorphism. The last event, resulting in the development of contrasting textures and compositional differences in apatite and monazite in the individual ore bodies, was driven by fluid flow enhanced by strain during tectonic deformation of the Boureéfjellet Shear Zone. In those ore bodies located in the highest grade levels of the Boureéfjellet Shear Zone, Cl-F apatite enriched in Sr and Mn as well as local S- and Sr-enriched monazite, argue for the presence of Ca-, Cl-, S-, Mn-, and Sr-bearing fluids, which overprinted the apatite and monazite during a presumed metamorphic event. Apatite and monazite are important petrogenetic indicators in ore prospecting (Mao et al., 2016). Hence a detailed understanding of their behaviour during fluid-rock interaction is crucial for helping to understand how ore deposits form and evolve over time.

This study represents a detailed first look at a series of small IOA ore bodies on Prins Karls Forland, Svalbard, and speculates as to their probable origin and subsequent metamorphic and metasomatic evolution involving limited fluid-aided mass transfer of REE, P, Cl, S, Sr, and Mn during the tectonothermal history of this part of the High Arctic. In this regard it also adds these ore bodies to the list of known IOA ore bodies worldwide and documents their unique characteristics relative to IOA ore bodies in general. To our knowledge these ores from Prins Karls Forland are the only Paleozoic IOA deposits so far described in the whole of the circum-Arctic region.

Declaration of Competing Interest

The authors declare that they have no known competing financial interests or personal relationships that could have appeared to influence the work reported in this paper.

Data availability

Data will be made available on request.

Acknowledgements

reviewers are thanked for critical and constructive assessment of previous versions of the manuscript which contributed to its improvement. The journal editor Jun Deng is acknowledged for handling of this paper.

Appendix A. Supplementary data

Supplementary data to this article can be found online at https://doi.org/10.1016/j.oregeorev.2023.105344.

References

Ague, J.J., 2014. Fluid flow in the deep crust. Treatise on geochemistry 2nd Edition, 4, 203-239.

Allen, R.L., Lundström, I., Ripa, M., Simeonov, A., Christofferson, H., 1996. Facies analysis of a 1.9 Ga, continental margin, back-arc, felsic caldera province with diverse ZnPb-Ag-(Cu-Au) sulfide and Fe oxide deposits, Bergslagen Region, Sweden. Econ. Geol. 91, 979–1006. https://doi.org/10.2113/gsecongeo.91.6.979.

Almeida, K.M.F., Jenkins, D.M., 2017. Stability field of the Cl-rich scapolite marialiate. Am. Mineral. 102, 2484–2493. https://doi.org/10.2138/am-2017-6132.

Almeida, K.M.F., Jenkins, D.M., 2019. Comparison between the stability fields of a Cl-rich scapolite and the end-member marialite. Am. Mineral. 104, 1788–1799. https://doi.org/10.2138/am-2019-6907.

Åmli, R., Griffin, W.L., 1975. Analysis of REE minerals using empirical correction factors. Am. Mineral. 60, 599–606.

Barnes, C.J. and Schneider, D.A., 2019. Late Cretaceous–Paleogene burial and exhumation history of the Southwestern Basement Province, Svalbard, revealed by zircon (U-Th)/He thermochronology. Piepjohn K, Strauss JV, Reinhardt L, McClelland WC (Ed) Circum-Arctic Structural Events: Tectonic Evolution of the Arctic Margins and Trans-Arctic Links with Adjacent Orogens. Geological Society of America, 541, 1–22.

Bekker, A., Slack, J.F., Planavsky, N., Krapež, B., Hofmann, A., Konhauser, K.O., Rouxel, O.J., 2010. Iron Formation: The Sedimentary Product of a Complex Interplay among Mantle, Tectonic, Oceanic, and Biospheric Processes. Econ. Geol. 105, 467–508. https://doi.org/10.2113/gsecongeo.105.3.467.

Belousova, E., Griffin, W., O'Reilly, S., Fisher, N., 2002. Apatite as an indicator mineral for mineral exploration: Trace-element compositions and their relationship to host rock type. J. Geochem. Explor. 76, 45–69. https://doi.org/10.1016/S0375-6742(02)00204-2.

Bonyadi, Z., Davidson, G.J., Mehrabi, B., Meffre, S., and Ghazban, F., 2011. Significance of apatite REE depletion and monazite inclusions in the brecciated Se–Chahun iron oxide–apatite deposit, Bafq district, Iran: insights from paragenesis and geochemistry. Chem. Geol., 281, 253–269. 10.1016/j.chemgeo.2010.12.013.

Broman, C., Nyström, J.O., Henríquez, F., Elfman, M., 1999. Fluid inclusions in magnetite– apatite ore from a cooling magmatic system at El Laco, Chile. Geol. Fören. Stockh. Förh. 121, 253–267. https://doi.org/10.1080/11035899901213253.

Broom-Fendley, S., Styles, M.T., Appleton, J.D., Gunn, A.G., Wall, F., 2016. Evidence for dissolution-reprecipitation of apatite and preferential LREE mobility in carbonatite-derived late-stage hydrothermal processes. Am. Mineral. 101, 596–611. https://doi.org/10.2138/am-2016-5502CCBY.

Broom-Fendley, S., Smith, M.P., Andrade, M.B., Ray, S., Banks, D.A., Loye, E., Atencio, D., Pickles, J.R., Wall, F., 2020. Sulfur-bearing monazite-(Ce) from the Eureka carbonatite, Namibia: oxidation state, substitution mechanism, and formation conditions. Mineral. Mag. 84, 35–48. https://doi.org/10.1180/mgm.2019.79.

Budzyń, B., Harlov, D.E., Kozub-Budzyń, G.A., Majka, J., 2017. Experimental constraints on the relative stabilities of the two systems monazite-(Ce) – allanite-(Ce) – fluorapatite and xenotime-(Y) – (Y, HREE)-rich epidote – (Y, HREE)-rich fluorapatite, in high Ca and Na-Ca environments under P-T conditions of 200–1000 MPa and 450–750 °C. Mineral. Petrol. 111, 183–217. https://doi.org/10.1007/s00710-016-0464-0.

Budzyń, B., Sláma, J., 2019. Partial resetting of U-Pb ages during experimental fluid-induced re-equilibration of xenotime. Lithos 346–347, 105163. https://doi.org/10.1016/j.lithos.2019.105163.

Carter, K.E., Dworkin, S.I., 1990. Channelized fluid flow through shear zones during fluid-enhanced dynamic recrystallization, Northern Apennines, Italy. Geology, 18, 720–723. doi: 10.1130/0091-7613(1990)018<0720:CFFTSZ>2.3.CO;2. Catlos, E., 2013. Generalizations about monazite: Implications for geochronologic studies. Am. Mineral., 98, 819–832. 10.2138/am.2013.4336.

Chakhmouradian, A.R., Ekater, P.R., Mitchell, R.H., 2002. Strontium-Apatite: New occurrences, and extent of Sr-for-Ca Substitution-group minerals. Can. Mineral. 40, 121–136.

Charlier, B., Grove, T.L., 2012. Experiments on liquid immiscibility along tholeiitic liquid lines of descent. Contrib. Mineral. Petrol. 164, 27–44. https://doi.org/10.1007/s00410-012-0723-y.

Charlier, B.T., Namur, O., Bolle, O., Latypov, R., Duchesne, J.C., 2015. Fe-Ti-V-P ore deposits associated with Proterozoic massif-type anorthosites and related rocks. Earth Sci. Rev. 141, 56–81. https://doi.org/10.1016/j.earscirev.2014.11.005.

Chen, W., Honghui, H., Bai, T., Jiang, S., 2017. Geochemistry of monazite within carbonatite related REE deposits. Resources 6, 51. https://doi.org/10.3390/resources6040051.

Cliff, R.A., Rickard, D., and Blake, K., 1990. Isotope systematics of the Kiruna magnetite ores, Sweden: Pt. 1. Age of the ore. Economic Geology, 85, 1770–1776. 10.2113/gsecongeo.85.8.1770.

Corriveau, L., Montreuil, J.-F., Potter, E., 2016. Alteration facies linkages among iron oxide–gold, iron oxide–apatite, and affiliated deposits in the Great Bear Magmatic Zone, Northwest Territories, Canada. Econ. Geol. 111, 2045–2072. https://doi.org/10.2113/econgeo.111.8.2045.

Crichton, W.A., Parise, J.B., Antao, S.M., Grzechnik, A., 2005. Evidence for monazite-, barite-, and AgMnO4 (distorted barite)-type structures of CaSO4 at high pressure and temperature. Am. Mineral. 90, 22–27.

Daliran, F., 2002. Kiruna-type iron oxide-apatite ores and apatites of the Bafq District, Iran, with an emphasis on the REE geochemistry of their apatites. In: Porter T.M. (ed) Hydrothermal Iron Oxide Copper-Gold and Related Deposits: A Global Perspective, PGC Publishing, Adelaide, 303–320.

Dallmann, W.K., 2020a. Notes on the geology of Prins Karls Forland: review and results of geological mapping and investigations in 2012–14. Norsk Polar Institutt Rapportserien 152.

Dallmann, W.K., Elvevold, S., Majka, J., Piepjohn, K., 2015. Tectonics and tectonothermal events. In Dallmann, WK.. (ed) Geoscience Atlas of Svalbard: Norwegian Polar Institute Report 148, 175–223.

Kośmińska, K., Spear, F.S., Majka, J., Faehrich, K., Manecki, M., Piepjohn, K., Dallmann, W., 2020. Deciphering late Devonian–early Carboniferous P–T–t path of mylonitized garnet-mica schists from Prins Karls Forland, Svalbard. Journal of Metamorphic Geology, 38, 471–493. 10.1111/jmg.12529.

Dare, S.A.S., Barnes, S.-J., Beaudoin, G., Méric, J., Boutroy, E., Potvin-Doucet, C., 2014. Trace elements in magnetite as petrogenetic indicators. Miner. Deposita 49, 785–796. https://doi.org/10.1007/s00126-011-0334-y.

Dare, S.A.S., Barnes, S.-J., Beaudoin, G., 2015. Did the massive magnetite "lava flows" of El Laco (Chile) form by magmatic or hydrothermal processes? New contraints from magnetite composition by LA-ICP-MS. Miner. Deposita 50, 607–617. https://doi.org/10.1007/s00126-014-0560-1.

Doherty, A.L., Webster, J.D., Goldoff, B.A., Piccoli, P.M., 2014. Partitioning behavior of chlorine and fluorine in felsic melt–fluid(s)–apatite systems at 50 MPa and 850–950 °C. Chem. Geol. 384, 94–109. https://doi.org/10.1016/j.chemgeo.2014.06.023.

Droop, G., 1987. A general equation for estimating Fe3+ concentrations in ferromagnesian silicates and oxides from microprobe analyses, using stoichiometric criteria. Mineral. Mag. 51, 431–435. https://doi.org/10.1180/minmag.1987.051.361.10.

Duchesne, J.C., 1999. Fe–Ti deposits in Rogaland anorthosites (South Norway): geochemical characteristics and problems of interpretation. Miner. Deposita 34, 182–198.

Dupuis, C., Beaudoin, G., 2011. Discriminant diagrams for iron oxide trace element fingerprinting of mineral deposit types. Miner. Deposita 46, 319–335. https://doi.org/10.1007/s00126-011-0334-y.

Dymek, R.F., Owens, B.E., 2001. Petrogenesis of apatite-rich rocks (nelsonites and oxide-apatite gabbronorites) associated with massif anorthosites. Econ. Geol. 96, 797–815.

Faryad, S.W., 2002. Metamorphic conditions and fluid compositions of scapolite-bearing rocks from the lapis lazuli deposit at Sare Sang, Afghanistan. J. Petrol. 43, 725–747. https://doi.org/10.1093/petrology/43.4.725.

Förster, H.J., 1998. The chemical composition of REE-Y-Th-U-rich accessory minerals in peraluminous granites of the Erzgebirge-Fichtelgebirge region, Germany, Part I: The monazite-(Ce)-brabantite solid solution series. American Mineralogist, 83, 259–27. 10.2138/am-1998-3-409.

Gee, D.G. and Teben'kov, A.M., 2004. Svalbard: A fragment of the Laurentian margin. In Gee DG Pease V (ed) The Neoproterozoic Timanide Orogen of Eastern Baltica Geological Society of London Memoir, 30, 191–206.

Geijer, P., 1931. The iron ores of the Kiruna type. Sveriges Geologiska Undersökning Serie C 367.

Geijer, P., 1910. Igneous rocks and iron ores of Kiirunavaara, Luossavaara and Tuolluvaara. Scientific and practical researches in Lapland arranged by Luossavaara-Kiirunavaara Aktiebolag. PhD Thesis Uppsala University.

Geijer, P., 1967. Internal features of the apatite-bearing magnetite ores. Sveriges Geologiska Undersökning Serie C 624, 32.

Gratz, R., Heinrich, W., 1997. Monazite–xenotime thermobarometry: experimental calibration of the miscibility gap in the binary system CePO4–YPO4. Am. Mineral. 82, 772–780. https://doi.org/10.1111/j.1525-1314.1997.t01-1-00052.x.

Harland, W.B., 1997. Geology of Svalbard. Geological Society of London. Memoir 17.

Harlov, D.E., Förster, H.J., 2003. Fluid-induced nucleation of REE phosphate minerals in apatite: nature and experiment. Part II. Fluorapatite. American Mineralogist, 88, 1209–1229. http://dx.doi.org/10.2138/am-2003-8-905.

Harlov, D.E., Andersson, U.B., Förster, H.-J., Broman, C., 2002. Apatite-monazite relations in the Kiirunavaara magnetite-apatite ore, northern Sweden. Chem. Geol. 191, 47–72. https://doi.org/10.1016/S0009-2541(02)00148-1.

Harlov, D.E., Wirth, R., Förster, H.J., 2005. An experimental study of dissolution-reprecipitation in fluorapatite: fluid infiltration and the formation of monazite. Contributions to Mineralogy and Petrology, 150, 268–286. doi.org/10.1007/s00410-005-0017-8.

Harlov, D.E., Meighan, C.J., Kerr, I.D., Samson, I.M., 2016. Mineralogy, chemistry, and fluid-aided evolution of the Pea Ridge Fe Oxide-(Y + REE) deposit, southeast Missouri, USA. Economic Geology, 111, 1963–1984. 10.2113/econgeo.111.8.1963.

Harlov, D.E., Hetherington, C.J., 2010. Partial high-grade alteration of monazite using alkali-bearing fluids: Experiment and nature. Am. Mineral. 95, 1105–1108.

Harlov, D., Wirth, R., Hetherington, C., 2007. The relative stability of monazite and huttonite at 300–900 °C and 200–1000 MPa: Metasomatism and the propagation of metastable mineral phases. Am. Mineral. 92, 1652–1664. https://doi.org/10.2138/am.2007.2459.

Harlov, D.E., Wirth, R., Hetherington, C.J., 2011. Fluid-mediated partial alteration in monazite: the role of coupled dissolution–reprecipitation in element redistribution

and mass transfer. Contrib. Miner. Petrol. 162, 329–348. https://doi.org/10.1007/s00410-010-0599-7.

Harlov, D.E., Wirth, R., 2012. Experimental incorporation of Th into xenotime at middle to lower crustal P-T utilizing alkali-bearing fluids. Am. Mineral. 97, 641–652. https://doi.org/10.2138/am.2012.3865.

Hawkins, T., Smith, M.P., Herrington, R.J., Maslennikov, V., Boyce, A.J., Jeffries, T., 2016. The geology and genesis of the iron skarns of the Turgai belt, northwestern Kazakhstan. Ore Geol. Rev. 85, 216–245. https://doi.org/10.1016/j.oregeorev.2015.10.016.

Henrichs, I.A., O'Sullivan, G., Chew, D.M., Mark, C., Babechuk, M.G., McKenna, C., Emo, R., 2018. The trace element and U-Pb systematics of metamorphic apatite. Chem. Geol. 483, 218–238. https://doi.org/10.1016/j.chemgeo.2017.12.031.

Hetherington, C.J., Harlov, D.E., 2008. Metasomatic thorite and uraninite inclusions in xenotime and monazite from granitic pegmatites, Hidra anorthosite massif, southwestern Norway: Mechanics and fluid chemistry. Am. Mineral. 93, 806–820. https://doi.org/10.2138/am.2008.2635.

Hetherington, C.J., Harlov, D.E., Budzyń, B., 2010. Experimental metasomatism of monazite and xenotime: mineral stability, REE mobility and fluid composition. Mineral. Petrol. 99, 165–184. https://doi.org/10.1007/s00710-010-0110-1.

Hjelle, A., Piepjohn, K., Saalmann, K., Salvigsen, K., Thiedig, F., Dallmann, W.K., 1999. Geological map of Svalbard 1:100,000 sheet A7G Kongsfjorden, Norsk Polarinstitutt Temakart 22.

Hou, T., Charlier, B., Namur, O., Schütte, P., Schwarz-Schampera, U., Zhang, Z., Holtz, F., 2017. Experimental study of liquid immiscibility in the Kiruna-type Vergenoeg iron–fluorine deposit, South Africa. Geochim. Cosmochim. Acta 203, 303–322.

Hou, T., Charlier, B., Holtz, F., Veksler, I., Zhang, Z., Thomas, R., Namur, O., 2018. Immiscible hydrous Fe–Ca–P melt and the origin of iron oxide-apatite ore deposits. Nature Communications, 9, P1415. 10.1038/srep01644 doi.org/.

Hu, H., Li, J.-W., Harlov, D.E., Lentz, D.R., McFarlane, C.R.M., Yang, Y.-H., 2019. A genetic link between iron oxide-apatite and iron skarn mineralization in the Jinniu volcanic basin, Daye district, eastern China: evidence from magnetite geochemistry and multi-mineral U-Pb geochronology. Geol. Soc. Am. Bull. 132, 899–917. https://doi.org/10.1130/B35180.1.

Huang, X.W., Boutroy, É., Makvandi, S., Beauduin, G., Corriveau, L., De Toni, A.F., 2019. Trace element composition of iron oxides from IOCG and IOA deposits: relationship to hydrothermal alteration and deposit subtypes. Miner. Deposita 54, 525–552. https://doi.org/10.1007/s00126-018-0825-1.

Jonsson, E., Persson-Nilsson, K., Hallberg, A., Högdahl, K., Troll, V.R., Weis, F., Harris, C., 2011. Oxygen isotopes and geochemistry of Palaeoproterozoic Kiruna-type deposits in the Bergslagen province, Sweden. 11th Biennial SGA meeting, Antofagasta, Chile. Abstract, 494–496.

Jonsson, E., Harlov, D.E., Majka, J., Hogdahl, K., Persson- Nilsson, K., 2016. Fluorapatite-monazite-allanite relations in the Grängesberg apatite-iron oxide ore district, Bergslagen, Sweden. American Mineralogist, 101, 1769–1782. 10.2138/am-2016-5655.

Jonsson, E., Troll, V.R., Högdahl, K., Harris, C., Weis, F., Nilsson, K.P., Skelton, A., 2013. Magmatic origin of giant central Swedish "Kiruna-type" apatite-iron oxide ores. Sci. Rep. 3 (1644), 1–8. https://doi.org/10.1038/srep01644.

Khoshnoodi, K., Behzadi, M., Gannadi-Maragheh, M., Yazdi, M., 2017. Alkali metasomatism and Th-REE Mineralization in the Choghart deposit, Bafq district, central Iran. Geologia Croatica 70, 53–69.

Klaver, M., Matveev, S., Berndt, J., Lissenberg, C.J., Vroon, P.Z., 2017. A mineral and cumulate perspective to magma differentiation at Nisyros volcano, Aegean arc. Contrib. Miner. Petrol. 172, 95. https://doi.org/10.1007/s00410-017-1414-5.

Knipping, J.L., Bilenker, L.D., Simon, A.C., Reich, M., Barra, F., Deditius, A.P., Lundstrom, C., Bindeman, I., Munizaga, R., 2015. Giant Kiruna-type deposits form by efficient flotation of magmatic magnetite suspensions. Geology 43, 591–594. https://doi.org/10.1130/g36650.1.

Knipping, J.L., Fiege, A., Simon, A., Oeser, M., Reich, M., Bilenker, L., 2019. In-situ iron isotope analyses reveal igneous and magmatic-hydrothermal growth of magnetite at the Los Colorados, Kiruna-type iron oxide-apatite deposit, Chile. Am. Mineral. 104, 471–484. https://doi.org/10.2138/am-2019-6623.

Kolker, A., 1982. Mineralogy and geochemistry of Fe–Ti oxide and apatite (nelsonite) deposits and evaluation of the liquid immiscibility hypothesis. Economic Geology, 77, 1146–1158.

Kośmińska, K., Schneider, D.A., Majka, J., Lorenz, H., Gee, D.G., Manecki, M., Barnes, C., 2015. Detrital zircon U-Pb geochronology of metasediments from southwestern Svalbard's Caledonian Province, EGU European Geosciences Union general assembly 2015. Geophys. Res. Abstr. 17, 11805.

Kośmińska, K., Spear, F.S., Majka, J., Faehnrich, K., Manecki, M., Piepjohn, K., Dallmann, W.K., 2020. Deciphering late Devonian-early Carboniferous P-T-t path of mylonitised garnet-mica schists from Prins Karls Forland, Svalbard. J. Metamorph. Geol. 38, 471–493. https://doi.org/10.1111/jmg.12529.

Kullerud, K., Erambert, M., 1999. Cl-scapolite, Cl-amphibole, and plagioclase equilibria in ductile shear zones at Nusfjord, Lofoten, Norway: implications for fluid compositional evolution during fluid–mineral interaction in the deep crust. Geochim. Cosmochim. Acta 63, 3829–3844.

Kullerud, K., Flaat, K., Davidsen, B., 2001. High-pressure fluid-rock reactions involving Cl-bearing fluids in lower-crustal ductile shear zone of the Flaktadøy basic complex, Lofoten, Norway. J. Petrol. 42, 1349–1372.

Kusebauch, C., John, T., Whitehouse, M.J., Klemme, S., Putnis, A., 2015. Distribution of halogens between fluid and apatite during fluid-mediated replacement processes. Geochim. Cosmochim. Acta 170, 225–246. https://doi.org/10.1016/j.gca.2015.08.023.

La Cruz, N., Simon, A., Wolf, A., Reich, M., Barra, F., Gagnon, J., 2019. The geochemistry of apatite from the Los Colorados iron oxide–apatite deposit, Chile: implications for

ore genesis. Miner. Deposita 54, 1145–1156. https://doi.org/10.1007/s00126-019-00861-z.

Laurent, A.T., Seydoux-Guillaume, A.M., Duchene, S., Bingen, B., Bosse, V., Datas, L., 2016. Sulphate incorporation in monazite lattice and dating the cycle of sulphur in metamorphic belts. Contrib. Miner. Petrol. 171, 94. https://doi.org/10.1007/s00410-016-1301-5.

Lester, G., Clark, A., Naslund, H., 2013. Experiments on liquid immiscibility in silicate melts with H₂O, P, S, F and Cl: Implications for natural magmas. Contrib. Miner. Petrol. 166, 329–349. https://doi.org/10.1007/s00410-013-0878-1.

Li, W., Audétat, A., Zhang, J., 2015. The role of evaporates in the formation of magnetite-apatite deposits along the Middle and Lower Yangtze River, China: Evidence from LA-ICP-MS analysis of fluid inclusions. Ore Geology Reviews, 67, 264–278, 10.1016/j.oregeorev.2014.12.003.

Lledo, H.L., Naslund, H.R., Jenkins, D.M., 2020. Experiments on phosphate–silicate liquid immiscibility with potential links to iron oxide apatite and nelsonite deposits. Contrib. Mineral. Petrol. 175, 111. https://doi.org/10.1007/s00410-020-01751-8.

Mair, P., Tropper, P., Harlov, D.E., Manning, C.E., 2017. The solubility of CePO₄ monazite and YPO₄ xenotime in KCl-H₂O fluids at 800 °C and 1.0 GPa: Implications for REE transport in high-grade crustal fluids. Am. Mineral. 102, 2457–2466. https://doi.org/10.2138/am-2017-6172.

Majka, J., Kośmińska, K., 2017. Magmatic and metamorphic events recorded within the Southwestern Basement Province of Svalbard. Arktos, 3, 5. 10.1007/s41063-017-0034-7.

Manby, G.M., 1983a. A reappraisal of chloritoid-bearing phyllites in the Forland Complex rocks of Prins Karls Forland, Spitsbergen. Mineral. Mag. 47, 311–318. https://doi.org/10.1180/minmag.1983.047.344.05.

Manby, G.M., 1983b. Primary scapolite from the foreland complex of Prins Karls Forland, Svalbard. Mineral. Mag. 47, 89–93. https://doi.org/10.1180/minmag.1983.047.342.20.

Manby, G.M., 1986. Mid-Palaeozoic metamorphism and polyphase deformation of the Forland Complex, Svalbard. Geol. Mag. 123, 651–663.

Mao, M., Rukhlov, A.S., Rowins, S.M., Spence, J., Coogan, L.A., 2016. Apatite trace element compositions: a robust new tool for mineral exploration. Econ. Geol. 111, 87–122. https://doi.org/10.2113/econgeo.111.5.1187.

Maraszewska, M., Manecki, M., Czerny, J., Schneider, D., Myhre, P.I., Faehnrich K., Barnes, C., 2016. Metagabbro associated with the shear zone on Prins Karls Forland (Svalbard, Arctic): EGU General Assembly, Vienna, Austria: Geophysical Research Abstracts 18.

McBirney, A.R., Nakamura, Y., 1973. Immiscibility in late-stage magmas of the Skaergaard intrusion. Carnegie Institute Washington Yearbook 73, 348–354.

McNaughton, N., Rasmussen, B., 2017. Geochemical characterisation of xenotime formation environments using U-Th. Chem. Geol. 484, 109–119. https://doi.org/10.1016/j.chemgeo.2017.08.016.

Ménard, J.J., 1995. Relationship between altered pyroxene diorite and the magnetite mineralization in the Chilean Iron Belt, with emphasis on the El Algarrobo iron deposits (Atacama region, Chile). Miner. Deposita 30, 268–274. https://doi.org/10.1007/bf00196362.

Nadoll, P., Angerer, T., Mauk, J.L., French, D., Walshe, J., 2014. The chemistry of hydrothermal magnetite: a review. Ore Geol. Rev. 61, 1–32.

Namur, O., Charlier, B., Holness, M.B., 2012. Dual origin of Fe–Ti–P gabbros by immiscibility and fractional crystallization of evolved tholeiitic basalts in the Sept Iles layered intrusion. Lithos 134, 100–114.

Naslund, H.R., 1983. The effect of oxygen fugacity on liquid immiscibility in iron-bearing silicate melts. Am. J. Sci. 283, 1034–1059.

Nisbet, H., Migdisov, A., Xu, H., Guo, X., van Hinsberg, V., Williams-Jones, A.E., Boukhalfa, H., Roback, R., 2018. An experimental study of the solubility and speciation of thorium in chloride-bearing aqueous solutions at temperatures up to 250 °C. Geochim. Cosmochim. Acta 239, 363–373.

Nutman, A.P., Friend, C.R.L., 2006. Petrography and geochemistry of apatites in banded iron formation, Akilia, W. Greenland: Consequences for oldest life evidence. Precambr. Res. 147, 100–106. https://doi.org/10.1016/j.precamres.2006.02.005.

Nyström, J.O., Henrıquez, F., 1994. Magmatic features of iron ores of the Kiruna-type in Chile and Sweden: ore textures and magnetite geochemistry. Econ. Geol. 89, 820–839. https://doi.org/10.2113/gsecongeo.89.4.820.

Oelkers, E.H., Poitrasson, F., 2002. An experimental study of the dissolution stoichiometry and rates of a natural monazite as a function of temperature from 50 to 230 °C and pH from 1.5 to 10. Chem. Geol. 191, 73–87. https://doi.org/10.1016/s0009-2541(02)00149-3.

Ondrejka, M., Uher, P., Pršek, J., Ozdín, D., 2007. Arsenian monazite-(Ce) and xenotime–(Y), REE arsenates and carbonates from the Tisovec-Rejkovo rhyolite, Western Carpathians, Slovakia: composition and substitutions in the (REE, Y)X₀4 system (X = P, As, Si, Nb, S). Lithos 95, 116–129. https://doi.org/10.1016/j.lithos.2006.07.019.

Oyarzun, R., Oyarzún, J., Ménard, J.J., Lillo, J., 2003. The Cretaceous iron belt of northern Chile: role of oceanic plates, a superplume event, and a major shear zone. Mineralium Deposita, 38, 640–646. 10.1007/s00126-003-0359-y.

Palma, G., Barra, F., Reich, M., Valencia, V., Simon, A.C., Vervoort, J., Leisen, M., Romero, R., 2019. Halogens, trace element concentrations, and Sr-Nd isotopes in apatite from iron oxide-apatite (IOA) deposits in the Chilean iron belt: evidence for magmatic and hydrothermal stages of mineralization. Geochim. Cosmochim. Acta 246, 515–540. https://doi.org/10.1016/j.gca.2018.12.019.

Palma, G., Barra, F., Reich, M., Simon, A.C., Romero, R., 2020. A review of magnetite geochemistry of Chilean iron oxide–apatite (IOA) deposits and its implications for ore-forming processes. Ore Geol. Rev. 126, 103748.

Perdahl, J.A., Frietsch, R., 1993. Petrochemical and petrological characteristics of 1.9 Ga old volcanics in northern Sweden. Precambr. Res. 64, 239–252. https://doi.org/10.1016/0301-9268(93)90079-h.

Philpotts, A.R., 1967. Origin of certain iron–titanium oxide and apatite rocks. Econ. Geol. 62, 303–315.

Pieczka, A., 2007. Beusite and unusual Mn-rich apatite from the Szklary granitic pegmatite, Lower Silesia, Southwestern Poland. Can. Mineral. 45, 901–914. https://doi.org/10.2113/gscanmin.45.4.901.

Poitrasson, F., Chenery, S., Bland, D.J., 1996. Contrasted monazite hydrothermal alteration mechanisms and their geochemical implications. Earth and Planetary Science Letters, 145, 79–96. http://doi.org/10.1016/s0012-821x(96)00193-8.

Pršek, J., Ondrejka, M., Bačík, P., Budzyń, B., Uher, P., 2010. Metamorphic-hydrothermal REE minerals in the Bacúch magnetite deposit, Western Carpathians, Slovakia: (Sr, S)-rich monazite-(Ce) and Nd-dominant digenite. Can. Mineral. 48, 81–94. https://doi.org/10.3749/canmin.48.1.81.

Putnis, A., 2002. Mineral replacement reactions: from macroscopic observations to microscopic mechanisms. Mineral. Mag. 66, 689–708. https://doi.org/10.1180/0026461026650056.

Putnis, A., 2009. Mineral replacement reactions. Rev. Mineral. Geochem. 70, 87–124.

Putnis, A., Austrheim, H., 2010. Fluid-induced processes: metasomatism and metamorphism. Geofluids 10, 254–269. https://doi.org/10.1111/j.1468-8123.2010.00285.x.

Rakovan, J.F., Hughes, J.M., 2000. strontium in the apatite structure: strontian fluorapatite and belovite-(Ce). Can. Mineral. 38, 839–845. https://doi.org/10.2113/gscanmin.38.4.839.

Rapp, J.F., Klemme, S., Butler, I.B., Harley, S.L., 2010. Extremely high solubility of rutile in chloride and fluoride-bearing metamorphic fluids: An experimental investigation. Geology 38, 323–326. https://doi.org/10.1130/G30753.1.

Richard, A., Montel, J.-M., Leborgne, R., Peiffert, C., Cuney, M., Cathelineau, M., 2015. Monazite alteration in $H_2O \pm HCl \pm NaCl \pm CaCl_2$ fluids at 150 °C and psat: implications for uranium deposits. Minerals 5, 693–706. https://doi.org/10.3390/min5040518.

Romer, R.L., Martinsson, O., Perdahl, J.A., 1994. Geochronology of the Kiruna iron ores and hydrothermal alterations. Economic Geology, 89, 1249–1261. 10.2113/gsecongeo.89.6.1249.

Schandl, E., Gorton, M., 2004. A textural and geochemical guide to the identification of hydrothermal monazite: criteria for selection of samples for dating epigenetic hydrothermal ore deposits. Economic Geology, 99, 1027–1035. 10.2113/gsecongeo.99.5.1027.

Schmidt, C., Rickers, K., Silverback, D.H., Huang, R., 2007. In situ synchrotron-radiation XRF study of REE phosphate dissolution in aqueous fluids to 800 °C. Lithos 95, 87–102. https://doi.org/10.1016/j.lithos.2006.07.017.

Schneider, D.A., Faehnrich, K., Majka, J., Manecki, M., 2019. $^{40}Ar/^{39}Ar$ geochronologic evidence of Eurekan deformation within the West Spitsbergen fold and thrust belt. Piepjohn, K., Strauss, JV., Reinhardt, L., and McClelland, W.C. (Ed) Circum-Arctic Structural Events: Tectonic Evolution of the Arctic Margins and Trans-Arctic Links with Adjacent Orogens. Geological Society of America, 541, 1–16. 10.1130/2018.2541(08).

Sepidbar, F., Ghorbani, G., Simon, A.C., Ma, J., Palin, R., Homam, S.M., 2022. Formation of the Chah-Gaz iron oxide-apatite ore (IOA) deposit, Bafq District, Iran: Constraints from halogens, trace element concentrations, and Sr-Nd isotopes of fluorapatite. Ore Geol. Rev. 140, 104599 https://doi.org/10.1016/j.oregeorev.2021.104.

Seydoux-Guillaume, A.-M., Paquette, J.-L., Wiedenbeck, M., Montel, J.-M., Heinrich, W., 2002. Experimental resetting of the U-Th–Pb systems in monazite. Chem. Geol. 191, 165–181. https://doi.org/10.1016/s0009-2541(02)00155-9.

Seydoux-Guillaume, A.-M., Montel, J.-M., Bingen, M., Bosse, V., de Perseval, P., Paquette, J.-L., Janots, E., Wirth, R., 2012. Low-temperature alteration of monazite: Fluid mediated coupled dissolution-reprecipitation, irradiation damage, and disturbance of the U-Pb and Th-Pb geochronometers. Chem. Geol. 330, 140–158. https://doi.org/10.1016/j.chemgeo.2012.07.031.

Sha, L.-K., Chappell, B.W., 1999. Apatite chemical composition, deter-mined by electron microprobe and laser-ablation inductively coupled plasma mass spectrometry, as a probe into granite petrogenesis. Geochim. Cosmochim. Acta 63, 3861–3881. https://doi.org/10.1016/s0016-7037(99)00210-0.

Shu, Q., Chang, Z., Mavrogenes, J., 2021. Fluid compositions reveal fluid nature, metal deposition mechanisms, and mineralization potential: An example at the Haobugao Zn-Pb skarn, China. Geology 49, 473–477.

Sillitoe, R.H., Burrows, D.R., 2002. New field evidence bearing on the origin of the El Laco magnetite deposit, northern Chile. Economic Geology, 97, 1101–1109. 10.2113/gsecongeo.98.7.1501.

Smith, D., 2014. Clinopyroxene precursors to amphibole sponge in arc crust. Nat. Commun. 5, 4329. https://doi.org/10.1038/ncomms5329.

Smith, M.P., Gleeson, S.A., Yardley, B.W.D., 2013. Hydrothermal evolution and metal transport in the Kiruna district, Sweden: contrasting metal behavior in aqueous, aqueous-carbonic brines. Geochimica Cosmochimica Acta 102, 89–112.

Szuszkiewicz, A., Pieczka, A., Gołębiowska, B., Dumańska-Słowik, M., Marszałek, M., Szełęg, E., 2018. Chemical composition of Mn- and Cl-rich apatites from the Szklary

pegmatite, Central Sudetes, SW Poland: taxonomic and genetic implications. Minerals 8, 350.

Taghipour, S., Kananian, A., Harlov, D., Oberhänsli, R., 2015. Kiruna-type iron oxide-apatite deposits, Bafq District, central Iran: fluid-aided genesis of fluorapatite-monazite-xenotime assemblages. Can. Mineral. 53, 479–496.

Tait, K., Ball, N.A., Hawthorne, F.C., 2015. Pieczkaite, ideally Mn5(PO4)3Cl, a new apatite-supergroup mineral from Cross Lake, Manitoba, Canada: Description and crystal structure. Am. Mineral. 100, 1047–1052.

Torab, F., Lehmann, B., 2007. Magnetite-apatite deposits of the Bafq District, central Iran: apatite geochemistry and monazite geochronology. Mineralogical Magazine, 71, 347–363. 10.1180/minmag.2007.071.3.347.

Tornos, F., Velasco, R.F., Hanchar, J., 2017. The magmatic to magmatic-hydrothermal evolution of the El Laco Deposit (Chile) and its implications for the genesis of magnetite-apatite deposits Economic Geology, 112, 1595–1628. 10.5382/econgeo.2017.4523.

Tornos, F., Velasco, R.F., Hanchar, J., 2016. Iron-rich melts, magmatic magnetite, and superheated hydrothermal systems: the El Laco deposit, Chile. Geology 44, 427–430. https://doi.org/10.1130/g37705.1.

Treloar, P.J., Colley, H., 1996. Variations in F and Cl concentrations in apatites from magnetite-apatite ores in northern Chile, and their ore-genetic implications. Mineralogical Magazine, 60, 285–301. 10.1180/minmag.1996.060.399.04.

Troll, V., Weis, F., Jonsson, E., Andersson, U., Majidi, A., Högdahl, K., Harris, C., Millet, M.A., Chinnasamy, S., Kooijman, E., and Persson-Nilsson, K., 2019. Global Fe–O isotope correlation reveals magmatic origin of Kiruna-type apatite-iron-oxide ores. Nature Communications, 10, 1712. 10.1038/s41467-019-09244-4.

Tropper, P., Manning, C.E., Harlov, D.E., 2011. Solubility of CePO4 monazite and YPO4 xenotime in H2O and H2O-NaCl at 800 °C and 1 GPa: implications for REE and Y transport during high-grade metamorphism. Chemical Geology, 282, 58–66. 10.1016/j.chemgeo.2011.01.009.

Tropper, P., Manning, C.E., Harlov, D.E., 2013. Experimental determination of CePO4 and YPO4 solubilities in H2O-NaF at 800 °C and 1 GPa: implications for rare earth element transport in high-grade metamorphic fluids. Geofluids 13, 372–380.

Tyrrell, G.W., 1924. The geology of Prince Charles Foreland, Spitsbergen. Royal Society of Edinburgh Transactions, 53, 443–478.

Visser, W., Koster van Groos, A.F., 1979. Effect of P_2O_5 and TiO_2 on liquid-liquid equilibria in the system K_2O-FeO-Al_2O_3-SiO_2. Am. J. Sci. 279, 970–988.

Wawrzenitz, N., Krohe, A., Rhede, D., Romer, R.L., 2012. Dating rock deformation with monazite: the impact of dissolution precipitation creep. Lithos 134–135, 52–74. https://doi.org/10.1016/j.lithos.2011.11.025.

Webster, J.D., Tappen, C.M., Mandeville, C.W., 2009. Partitioning behavior of chlorine and fluorine in the system apatite-melt-fluid. II: Felsic silicate systems at 200 MPa. Geochim. Cosmochim. Acta 73, 559–581. https://doi.org/10.1016/j.gca.2008.10.034.

Williams, M.L., Jercinovic, M.J., Harlov, D.E., Budzyń, B., Hetherington, C.J., 2011. Resetting monazite ages during fluid-related alteration. Chem. Geol. 283, 218–225. https://doi.org/10.1016/j.chemgeo.2011.01.019.

Williams, P.J., 2010. Classifying IOCG deposits. In: Corriveau, L. and Mumin, H. (eds) Exploring for iron oxide copper–gold deposits: Canada and global analogues. Geological Association of Canada Short Course Notes, 20, 13–22.

Williams-Jones, A.E., Heinrich, C.A., 2005. Vapor transport of metals and the formation of magmatic-hydrothermal ore deposits. Econ. Geol. 100, 1287–1312. https://doi.org/10.2113/gsecongeo.100.7.1287.

Xing, Y., Mei, Y., Etschmann, B., Liu, W., Brugger, J., 2018. Uranium transport in F-Cl-bearing fluids and hydrothermal upgrading of U-Cu Ores in IOCG Deposits. Geofluids 18, 1–22. https://doi.org/10.1155/2018/6835346.

Yardley, B.W.D., Cleverley, J.S., 2013. The role of metamorphic fluids in the formation of ore deposits. Geological Society of London, Special Publications 393, 117–134. https://doi.org/10.1144/SP393.5.

Yardley, B.W.D., Graham, J.T., 2002. Origins of salinity in metamorphic fluids. Geofluids 2, 249–256. https://doi.org/10.1046/j.1468-8123.2002.00042.x.

Zhang, F., Li, W., White, N., Zhang, L., Qiao, X., Yao, Z., 2020. Geochemical and isotopic study of metasomatic apatite: Implications for gold mineralization in Xindigou, northern China. Ore Geol. Rev. 127, 103853.

Zhang, W., Shao, J., Wang, R., Xu, X., Che, X., Yang, Y., 2011. Sr-rich apatite from the Dangzishan leucitite-ijolite xenoliths (Heilongjiang Province): Mineralogy and mantle-fluid metasomatism. China Science Bulletin 56, 53–63. https://doi.org/10.1007/s11434-010-4228-7.

Zhou, R.J., Wen, G., Li, J.W., 2022. Apatite chemistry as a petrogenetic–metallogenic indicator for skarn ore-related granitoids: an example from the Daye Fe–Cu–(Au–Mo–W) district, Eastern China. Contrib. Miner. Petrol. 177, 23. https://doi.org/10.1007/s00410-022-01890-0.

Zhu, C., Sverjensky, D.A., 1991. Partitioning of F-Cl-OH between minerals and hydrothermal fluids. Geochim. Cosmochim. Acta 55, 1837–1858. https://doi.org/10.1016/0016-7037(91)90028-4.